Two-phase Lattice Boltzmann modelling of streaming potentials: influence of the air–water interface on the electrokinetic coupling

Eve-Agnès Fiorentino, Renaud Toussaint, Laurence Jouniaux

Geophysical Journal International

Geophys. J. Int. (2017) **208,** 1139–1156
Advance Access publication 2016 November 5
GJI Marine geosciences and applied geophysics

doi: 10.1093/gji/ggw417

Two-phase Lattice Boltzmann modelling of streaming potentials: influence of the air–water interface on the electrokinetic coupling

Eve-Agnès Fiorentino, Renaud Toussaint and Laurence Jouniaux

Institut de Physique du Globe de Strasbourg, UMR 7516*, Université de Strasbourg/EOST, CNRS,* 5 *rue René Descartes, F-*67084 *Strasbourg cedex, France.*
E-mail: eafiorentino@unistra.fr

Accepted 2016 November 3. Received 2016 October 11; in original form 2016 April 22

SUMMARY

The streaming potential phenomenon is an electrokinetic effect that occurs in porous media. It is characterized by an electrokinetic (EK) coefficient. The aim of this paper is to simulate the EK coefficient in unsaturated conditions using the Lattice Boltzmann method in a 2-D capillary channel. The multiphase flow is simulated with the model of Shan & Chen. The Poisson–Boltzmann equation is solved by implementing the model of Chai & Shi. The streaming potential response shows a non-monotonous behaviour due to the combination of the increase of charge density and decrease of flow velocity with decreasing water saturation. Using a ζ potential of −20 mV at the air–water interface, an enhancement of a factor 5–30 of the EK coefficient, compared to the saturated state, can be observed due to the positive charge excess at this interface which is magnified by the fluid velocity away from the rock surface. This enhancement is correlated to the fractioning of the bubbles, and to the dynamic state of these bubbles, moving or entrapped in the crevices of the channel.

Key words: Numerical solutions; Electrical properties; Hydrogeophysics.

1 INTRODUCTION

The streaming potential (SP) phenomenon is an electrokinetic effect which arises when an electrolyte flows in a porous medium. When the surface of the solid material composing the matrix of the porous medium is electrically charged, the presence of an electrical double layer at the interface between the fluid and the solid phase creates a streaming current, counterbalanced by a conduction current, leading to a measurable electrical voltage. This electrokinetic coupling is at the origin of the self-potential and seismo-electromagnetic conversions used in earth sciences as geophysical tools for the subsurface imaging. These methods offer a non-invasive structure characterization of the near-surface in terms of fluids (water, oil, gas), and are developed for characterizing water resources, monitoring contaminated aquifers, and monitoring natural hazards which can be controlled by the role of water and ice.

The self-potential method is a passive geophysical method which consists in measuring the natural electric field on the earth surface, whereas the seismo-electromagnetic conversions are detected by measuring the electromagnetic field induced by a seismic wave propagation. These techniques have a variety of geophysical applications related to multiphase flows such as the study of the vadose zone (Thony *et al.* 1997; Warden *et al.* 2013; Jougnot *et al.* 2015), the estimate of the water retention parameters (Darnet & Marquis 2004), the estimate of the dispersivity (Straface & De Biase 2013), the monitoring of ground water flow (Perrier *et al.* 1998; Jouniaux *et al.* 1999; Doussan *et al.* 2002), the detection of deep fluid flow after stimulation of geothermal reservoir (Darnet *et al.* 2006), or the daily SP variations produced by capillary flow in the non-saturated zone (Perrier & Morat 2000). Groundwater flow paths and hydraulic properties of an aquifer can be inferred by SP measurements during pumping tests, especially the hydraulic conductivity, the aquifer thickness and the electrokinetic coupling (Darnet *et al.* 2003; Rizzo *et al.* 2004; Maineult *et al.* 2008; Straface *et al.* 2010; Chidichimo *et al.* 2015). On active volcanic areas, the upward hydrothermal flow can be characterized through SP observations usually showing positive anomalous electric signals (Hase *et al.* 2005; Mauri *et al.* 2010; Brothelande *et al.* 2014). These techniques are also of high interest for the hydrocarbon recovery (Saunders *et al.* 2006; Forté & Bentley 2013), the detection of contaminated aquifers (Naudet *et al.* 2004; Maineult *et al.* 2006; Minsley *et al.* 2007; Giampaolo *et al.* 2014), the monitoring of CO_2 storage (Zyserman *et al.* 2015), the prospection of ice-water interfaces (Kallay *et al.* 2003; Kulessa *et al.* 2006), and the mapping of water flow below glaciers (Kulessa *et al.* 2003). The knowledge of the unsaturated electrokinetic coupling is therefore essential, so that it can be included in the models for a better understanding of the observations.

The electrical double layer, which is at the origin of these phenomena, stems from the charge of the mineral when an electrolyte is in contact with the rock (Davis *et al.* 1978). This potential is negative for quartz at pH >3. The local electroneutrality in the immediate vicinity of the rock is satisfied thanks to an excess of positive ions adsorbed and immobile. The amount of positive charges in the electrolyte decays as getting away from the surface of the capillary, until both negative and positive species are found in equal proportion. The portion of capillary containing the positive charge excess is called the diffuse layer.

The SP phenomenon is characterized thanks to an electrokinetic (EK) coefficient, that is equal to the ratio of the potential difference δV created by the displacement of the positive charge excess, on the pressure difference δP that allows to generate the flow

$$C_{\mathrm{EK}} = \frac{\delta V}{\delta P}. \tag{1}$$

The behaviour of the EK coefficient in unsaturated conditions is a debated question which is the topic of numerous studies. Wurmstich & Morgan (1994) proposed an enhancement factor of the EK coefficient with decreasing water saturation, by assuming that air forms bubbles in the medium. They assumed for this, that the bubbles decrease much less the water flow (streaming current) than they affect the conduction current through the decrease of electrical conductivity. The presence of bubbles was investigated theoretically and experimentally by Sherwood (2007), Xie *et al.* (2010), Sherwood *et al.* (2013), who measured an enhancement of the output power caused by an increase of resistivity and streaming current. Perrier & Morat (2000) suggested that the EK coefficient could scale with the relative permeability and with the inverse of relative conductivity, leading to a decreasing trend with decreasing water saturation. This scaling was further developed by Linde *et al.* (2007) and Revil *et al.* (2007) who introduced a scaling of the charge density with the inverse of the saturation. Using a volume-average approach, they obtained a monotonous decreasing trend with decreasing water saturation. Laboratory measurements at various saturations (Guichet *et al.* 2003; Revil & Cerepi 2004; Revil *et al.* 2007; Vinogradov & Jackson 2011) lead to a constant or decreasing trend with decreasing water saturation. Continuous records of the EK coefficient as a function of water saturation made by Allègre *et al.* (2010) exhibited a non-monotonous behaviour, with a great enhancement compared to the saturated state, coherent with other data (Allègre *et al.* 2011). Allègre *et al.* (2012) modelled Richards' equation for the hydrodynamics and Poisson's equation for the electrical potential with a 1-D finite element method, and concluded, based on their previous experiments, that the unsaturated electrokinetic coefficient should be non-monotonous. An extension of the model of capillary tubes of Ishido & Mizutani (1981) to the case where each capillary can have a different radius was developed by Jackson (2008, 2010). This model predicts a monotonous decreasing EK coefficient with decreasing water saturation in the water-wet case and a non-monotonous and enhanced behaviour of the EK coefficient in the oil-wet case if the diffuse layer is not negligible compared to the capillary radius. Considering the same scaling of the charge density as the one used by Linde *et al.* (2007) and Revil *et al.* (2007), but using a flux-averaging approach, Jougnot *et al.* (2012) obtained an enhancement of three to four orders of magnitude of the steaming potential response of a rainfall event, thanks to a better consideration of the charge density and velocity distributions in the pore space. Their model predicts a non-monotonous behaviour of the EK coefficient with an enhancement from two to five times the value at water saturation under certain conditions.

Most of these models have in common (i) to assume that the phases are continuous at the scale of a representative elementary volume, and (ii) to neglect the charge density associated to the air–water interface. Recently, some studies suggested that the polarization of this air–water interface could play a key role in the SP response (Allègre *et al.* 2014, 2015). The aim of this paper is to investigate the behaviour of the EK coefficient using Lattice Boltzmann (LB) simulations, when the non-wetting phase is discontinuous at the scale of the capillary, and when the contribution of the air–water interface is not considered as negligible compared to the charge density associated to the fluid-rock interface.

The LB method is a computational fluid dynamics technique that allows to simulate advection and diffusion phenomena. It is an increasingly popular technique allowing to accurately mimic the multiphase dynamics at the pore scale, without need to track the interface between the fluids in a dynamic calculation (Yang *et al.* 2001b; Van der Graaf *et al.* 2006; Pride *et al.* 2008; Aursjø *et al.* 2011). As in monophasic conditions, the LB simulations of multiphase flows can be coupled to the LB resolution of electric, thermal or chemical problems (Zhang & Kwok 2005; Gong *et al.* 2010; Parmigiani *et al.* 2011; Misztal *et al.* 2015). In this study, EK coefficients are simulated for various saturations using two independent LB algorithms solving the fluid velocity, and the potential resulting from the conduction currents, taking into account the fluid-rock and fluid-fluid interfaces. We will focus on a two-phase flow problem where one of the phases, like air, is an electrical insulator. The EK coefficient will be assessed when air remains trapped in the crevices of the irregularly shaped pore, and when air flows by forming bubbles dragged with the flow.

2 METHOD

The algorithm implemented to simulate the SP phenomenon was presented by Fiorentino *et al.* (2016) in monophasic conditions. The basic idea is to simulate the flow of the electrolyte using a LB algorithm, the charge density deriving from the potential given by the Poisson–Boltzmann equation using another LB algorithm, and to multiply these quantities through the computation of the electric field at each site of the lattice. The improvement brought in this paper is the adjunction of an immiscible phase. The literature reports three main families of methods allowing to model multiphase/multicomponent flows using LB principles: the colour gradient model (Gunstensen *et al.* 1991), the Shan-Chen model (Shan & Chen 1993) and the free energy model (Swift *et al.* 1995, 1996). The Shan-Chen model appears to be the most employed one due to its simplicity and computational efficiency. It is thus very well documented. As in one-phase conditions, the electrical potential is solved by implementing the model of Chai & Shi (2008). The following sections introduce the equations constituting these models and how they are used to compute the electrical field giving the EK coefficient in unsaturated conditions.

2.1 Modelling of the two-phase flow

The fundamental principle of the LB method is the use of numerical fluid particles that propagate and collide in a fixed number of directions. In a 2-D system, the number of directions needed to reproduce the behaviour of a fluid amounts to 9. The matrix of the particles velocities along these directions reads

$$\boldsymbol{c}_V = c_V \begin{bmatrix} 0 & 1 & 0 & -1 & 0 & 1 & -1 & -1 & 1 \\ 0 & 0 & 1 & 0 & -1 & 1 & 1 & -1 & -1 \end{bmatrix} \tag{2}$$

where $c_V = dx_V/dt_V$ is the ratio between the space and the time steps. The time step is provided by the relationship $dt_V = \frac{\nu^{ad}}{\nu} dx_V^2$, where ν is the kinematic viscosity of the fluid and ν^{ad} is the adimensional kinematic viscosity, fixed by the user. The space step is the distance between two lattice sites, given by $dx_V = 2R/(ny_V - 1)$ if R is the radius of the channel and ny_V the number sites discretizing the capillary diameter. The number of sites in the direction parallel to the flow is nx_V. Starting from now and until the end of this section,

all the quantities are adimensional (see Table A1 in the Appendix for a summary of the variables). Times will be expressed in time steps (ts), lengths in lattice units (lu) and masses in mass units (mu). The physical mass is obtained by multiplying the mass in mu by $\mu_0 \, dx_V^3$ where μ_0 is a reference volumetric mass density, chosen here as the water mass density.

Let f_i^λ be the probability of presence of a particle of the fluid component λ in the direction i. The local adimensional density of λ is defined as

$$\rho_\lambda = \sum_i f_i^\lambda \tag{3}$$

and the local momentum of λ as

$$\rho_\lambda \boldsymbol{u}_\lambda = \sum_i \boldsymbol{c}_{Vi} f_i^\lambda. \tag{4}$$

Each distribution f_i^λ evolves following the propagation-relaxation equation

$$f_i^\lambda(\boldsymbol{x} + \boldsymbol{c}_{Vi} dt, t + dt) - f_i^\lambda(\boldsymbol{x}, t) = \Omega(\boldsymbol{x}, t) \tag{5}$$

where $\Omega(\boldsymbol{x}, t) = -\frac{1}{\tau_\lambda}(f_i^\lambda(\boldsymbol{x}, t) - f_i^{\lambda,\mathrm{eq}}(\boldsymbol{x}, t))$. This equation expresses that at each time step the distribution at $\boldsymbol{x}$ is advected to a position $\boldsymbol{x} + \boldsymbol{c}_{Vi} dt_V$, and interacts with the other particles to converge towards equilibrium. The left-hand side is generally called the streaming step, and the right-hand side the collision step. τ_λ is a relaxation time related to the kinematic viscosity through the relationship $\tau_\lambda = 3\nu^{ad} + 0.5$ (Wolf-Gladrow 2005). τ_λ controls the amount of collisions between the particles, and thus the rheology of the fluid. It must be >0.5 to have a positive viscosity, and avoid stability problems.

The equilibrium distribution function $f_i^{\lambda,\mathrm{eq}}$ is expressed as a function of an equilibrium velocity u_λ^{eq}

$$f_i^{\lambda,\mathrm{eq}} = w_i \rho_\lambda \left[1 + 3\frac{\boldsymbol{c}_{Vi} \cdot \boldsymbol{u}_\lambda^{\mathrm{eq}}}{c_V^2} + \frac{9}{2}\frac{(\boldsymbol{c}_{Vi} \cdot \boldsymbol{u}_\lambda^{\mathrm{eq}})^2}{c_V^4} - \frac{3}{2}\frac{\boldsymbol{u}_\lambda^{\mathrm{eq}2}}{c_V^2} \right] \tag{6}$$

with $w_i = 4/9$ for $i = 0$, $w_i = 1/9$ for $i = \{1,2,3,4\}$ and $w_i = 1/36$ for $i = \{5,6,7,8\}$. The equilibrium velocity $\boldsymbol{u}_\lambda^{\mathrm{eq}}$ is the sum of a composite macroscopic velocity of the mixture denoted $\boldsymbol{u}'$ and an interaction force term $\boldsymbol{F}_\lambda = \boldsymbol{F}_\lambda^{\mathrm{coh}} + \boldsymbol{F}_\lambda^{\mathrm{ads}}$ which is the sum of the fluid–fluid and fluid–solid interaction forces:

$$\boldsymbol{u}_\lambda^{\mathrm{eq}} = \boldsymbol{u}' + \frac{\tau_\lambda \boldsymbol{F}_\lambda}{\rho_\lambda} \tag{7}$$

with

$$\boldsymbol{u}' = \frac{\sum_\lambda \frac{\rho_\lambda \boldsymbol{u}_\lambda}{\tau_\lambda}}{\sum_\lambda \frac{\rho_\lambda}{\tau_\lambda}}. \tag{8}$$

$\boldsymbol{F}_\lambda^{\mathrm{coh}}$ is an interparticle force allowing to introduce the cohesion of the phases. The force exercised locally by the fluid component $\bar{\lambda}$ on the fluid component λ is proportional to the local density of λ multiplied by the sum of the densities of $\bar{\lambda}$ over the 8 neighbouring sites:

$$\boldsymbol{F}_\lambda^{\mathrm{coh}}(\boldsymbol{x}, t) = -\rho_\lambda(\boldsymbol{x}, t) G^{\mathrm{coh}} \sum_i w_i \rho_{\bar{\lambda}}(\boldsymbol{x} + \boldsymbol{c}_{Vi} dt_V, t) \boldsymbol{c}_{Vi}. \tag{9}$$

The parameter G^{coh} controls the magnitude of the repulsion between λ and $\bar{\lambda}$, and thus the interfacial tension between the phases. If G^{coh} is too low, the phase separation does not occur. A high G^{coh} decreases the solubility of the fluids within each other and allows to minimize the thickness of the fluid interface. However, stability problems occur when it is too high.

The force allowing to create the fluid-solid adhesion is similar to the force creating the interparticle interaction, but instead of summing the density of the neighbouring sites, the force is computed by summing a flag variable s_i such as $s_i = 1$ if $\boldsymbol{x} + \boldsymbol{c}_{Vi} dt_V$ is solid, and $s_i = 0$ otherwise (Martys & Chen 1996):

$$\boldsymbol{F}_\lambda^{\mathrm{ads}}(\boldsymbol{x}, t) = -\rho_\lambda(\boldsymbol{x}, t) G_\lambda^{\mathrm{ads}} \sum_i w_i s_i(\boldsymbol{x} + \boldsymbol{c}_{Vi} dt_V, t) \boldsymbol{c}_{Vi}. \tag{10}$$

The difference $G_\lambda^{\mathrm{ads}} - G_{\bar{\lambda}}^{\mathrm{ads}}$ allows to tune the wetting properties of the fluids. G^{ads} is generally chosen positive for the wetting fluid and negative for the non-wetting fluid. Huang *et al.* (2007) proposed a straightforward translation of Young's equation using the interfacial tensions and a density factor $[\rho_\lambda - \rho_{\bar{\lambda}}]/2$:

$$\cos\theta = \frac{G_{\bar{\lambda}}^{\mathrm{ads}} - G_\lambda^{\mathrm{ads}}}{G^{\mathrm{coh}} \frac{\rho_\lambda - \rho_{\bar{\lambda}}}{2}}. \tag{11}$$

They found that G_λ^{ads} and $G_{\bar{\lambda}}^{\mathrm{ads}}$ can be chosen in equal magnitude, but that the correspondence between the contact angle computed from eq. (11) and the contact angle measured graphically is slightly more accurate with $G_\lambda^{\mathrm{ads}} \approx -G_{\bar{\lambda}}^{\mathrm{ads}} + 0.1$.

Due to the diffusive nature of the interfaces modelled with the interparticle force, a fraction of each phase is present at each lattice site, even if one is always dominant far from the interfacial area. The local total density of the mixture is given by

$$\rho = \sum_\lambda \rho_\lambda \tag{12}$$

and the total velocity by

$$\boldsymbol{u} = \frac{1}{\rho}\left[\sum_\lambda \sum_i \boldsymbol{c}_{Vi} f_i^\lambda + \frac{1}{2}\sum_\lambda \boldsymbol{F}_\lambda \right]. \tag{13}$$

The physical velocity of the fluid is obtained by multiplying u with the lattice velocity c_V.

In the following simulations, the two fluids are given the same viscosity $\eta = 1.002$ mPa s (water viscosity) and same mass density $\mu = 10^3$ kg m^{-3} (water mass density). Indeed, the high density and viscosity contrasts that occur when modelling liquid-gas mixtures constitute a challenge in the LB community that is out of the scope of this paper. Both phases will be given the same viscosity, and thus, the same relaxation times τ_λ (see for instance, Yang *et al.* 2001b; Zhang & Kwok 2005; Qian *et al.* 2006; Gong *et al.* 2010). Merely, the component representing water will be the wetting component and the phase representing air the non-wetting component.

2.2 Driving force

The driving force in the Shan-Chen model is classically incorporated in the equilibrium velocity with the other forces responsible for the separation of the phases. It has been argued, however, that this way to create the flow is strictly valid for $\tau = 1$ (e.g., Yang & Boek 2013). The flow is here generated by incorporating a term Ω' at the right-hand side of eq. (5) (see Wolf-Gladrow (2005) and also Buick & Greated (2000)):

$$\Omega_i'(\boldsymbol{x}, t) = \frac{dt_V \boldsymbol{c}_{Vi}}{12 c_V^2 \mu_0}[\boldsymbol{K}(\boldsymbol{x}, t) + \boldsymbol{K}(\boldsymbol{x} + \boldsymbol{c}_{Vi} dt_V, t + dt_V)] \tag{14}$$

where $\boldsymbol{K} = \nabla P$ is the pressure gradient in physical units. $\|\nabla P\| = \delta P / L$ where L is the channel's length in m, and δP the pressure drop along the channel in Pa. δP determines the strength of the flow.

In this study the flow velocity is used to counteract an artefact that plagues the multiphase LB simulations. This artefact, called the

spurious currents, is the occurrence of non-physical velocities at the interface between the immiscible fluids. This phenomenon has been extensively studied in the literature (see Connington & Lee (2012) for a review). Many efforts have been made to understand it, but it is still very hard or impossible to remove completely. A possible means to decrease the impact of these spurious currents is to generate a flow that is sufficiently rapid to make the relative importance of these anomalous velocities not too big (e.g. Bao & Schaefer 2013). In this study, the δP will be set to very large values so that the main current's magnitude will minimize the contribution of the spurious currents.

2.3 Computation of the electrical potential

The electrical potential, denoted ψ, is computed by implementing the model of Chai & Shi (2008), in a lattice of ny_P sites along the distance between the rock surfaces, and nx_P sites in the direction parallel to these surfaces. The resolution of the Poisson–Boltzmann equation is similar to the resolution of a diffusion equation, for which the number of directions available to the particles amounts to 5. The matrix of the particle velocities along these directions is

$$\boldsymbol{c_P} = c_P \begin{bmatrix} 0 & 1 & 0 & -1 & 0 \\ 0 & 0 & 1 & 0 & -1 \end{bmatrix}, \tag{15}$$

where $c_P = dx_P/dt_P$ is the lattice velocity, dt_P is the time step and $dx_P = 2R/(ny_P - 1)$ the space step.

By denoting h_i the particle distributions allowing to compute the electrical potential, ψ is given by

$$\psi(\boldsymbol{x}, t) = \sum_i h_i(\boldsymbol{x}, t). \tag{16}$$

The particle distributions h_i follow the same propagation-relaxation equation as eq. (5)

$$h_i(\boldsymbol{x} + \boldsymbol{c_P}_i dt, t + dt) - h_i(\boldsymbol{x}, t) = \Omega_i(\boldsymbol{x}, t) + \Omega_i'(\boldsymbol{x}, t). \tag{17}$$

The collision operator Ω_i defined as

$$\Omega_i(\boldsymbol{x}, t) = -\frac{1}{\tau_P}(h_i(\boldsymbol{x}, t) - h_i^{\mathrm{eq}}(\boldsymbol{x}, t)), \tag{18}$$

is a function of the equilibrium distributions h_i^{eq}

$$h_i^{\mathrm{eq}}(\boldsymbol{x}, t) = \begin{cases} \frac{w_0 - 1}{1 - w_0} \sum_{i=1}^{5} h_i(\boldsymbol{x}, t) & \text{if} \quad i = 0 \\ \frac{w_i}{1 - w_0} \sum_{i=1}^{5} h_i(\boldsymbol{x}, t) & \text{if} \quad i = \{1, 2, 3, 4\} \end{cases} \tag{19}$$

where the w_i are $w_i = 0$ for $i = 0$ and $w_i = 1/4$ for $i = \{1, 2, 3, 4\}$.

The term Ω_i' introduces the electrical source

$$\Omega_i'(\boldsymbol{x}, t) = dt_P w_i \Theta(\boldsymbol{x}, t) D. \tag{20}$$

D is an artificial diffusion coefficient given by

$$D = \alpha c_P^2 \left(\frac{1}{2} - \tau\right) dt_P \tag{21}$$

with $\alpha = \frac{1}{2}$ in this 2-D system. Θ is the right-hand side of the Poisson–Boltzmann equation:

$$\Theta(\boldsymbol{x}, t) = \frac{\rho_e(\boldsymbol{x}, t)}{\varepsilon_r \varepsilon_0}. \tag{22}$$

We calculate the value of ρ_e thanks to the local concentrations of the species denoted $C_i(\boldsymbol{x}, t)$:

$$\rho_e(\boldsymbol{x}, t) = \sum_i^n \rho_i(\boldsymbol{x}, t) = \sum_i^n e z_i C_i(\boldsymbol{x}, t), \tag{23}$$

where $e = 1.6021\,10^{-19}$ C is the fundamental charge, z_i is the valence of the species i and C_i its concentration in ions m^{-3}. The species concentrations are functions of the local value of the electrical potential:

$$C_i(\boldsymbol{x}, t) = C_i^{\infty} \exp\left(-\frac{z_i e \psi(\boldsymbol{x}, t)}{k_{\mathrm{B}} T}\right), \tag{24}$$

where $k_{\mathrm{B}} = 1.3806\,10^{-23}$ J K^{-1} is the Boltzmann constant, T is the temperature in K and C_i^{∞} is the species concentration when $\psi = 0$, like out of the rock sample of far from the rock surfaces.

To sum up, the medium is initialized by setting $\rho_e(\boldsymbol{x}, t) = \sum_i^n e z_i C_i^{\infty}$ everywhere. The electrical potential ψ is calculated as a function of ρ_e thanks to eqs (16)–(22). The concentrations are calculated as a function of ψ using eq. (24). Then ρ_e is updated with the new values of C_i according to eq. (23). At each time step the potential evolves because some sites have a fixed potential (rock and fluid-fluid interfaces) which 'diffuse' to the neighbouring sites. To assign a fixed potential ζ to a particular point $\boldsymbol{x}$, the particle distributions of point $\boldsymbol{x}$ are forced to keep the value

$$h_i(\boldsymbol{x}, t) = \zeta w_i. \tag{25}$$

The procedure is repeated until the electrical potential is stabilized (see next section).

It can be shown easily by combining eqs (20) and (21) that the time step dt_P simplifies with c_P, so that no tuning of dt_P is needed. The space step dx_P is fixed so as to describe the diffuse layer precisely. A good precision is reached when $d/dx_P \sim 60$ (see Fiorentino *et al.* 2016). The dimensionless relaxation time is fixed at $\tau_P = 1$ like in the simulation tests carried out by Chai & Shi (2008). The calculation is directly made in physical units, with double precision variables.

2.4 Computation of the EK coefficient

In the monophasic situation, both algorithms (flow velocity and potential) were computed at the same time. The convergence of the algorithm was evaluated by calculating the relative change of C_{EK} between each 10 steps. The origin of the electrical potential was located in the rock sites, which had a fixed position. In this study, the EK coefficient is computed in the presence of two phases in three situations: (i) the phases flow in parallel, (ii) the non-wetting phase is entrapped in the crevices of the pore, and (iii) the non-wetting phase flows as one or several bubbles. The source of the potential is located not only in the rock, but also at the fluid-fluid interfaces which do not have a fixed position. The Poisson–Boltzmann equation cannot converge if the source of the potential moves at each time step. Both parts of the algorithm (velocity and potential) cannot be solved simultaneously.

In this study, the velocity field is calculated in a preliminary stage. At the initial state, the medium is immobile. Then the velocity increases until an equilibrium is reached. The convergence of the velocity is assessed using the relative change of the fluid velocity averaged over the whole medium. Once the average velocity is stabilized, a 'snapshot' of the interfaces locations is made. The fluid-fluid interfaces are tracked by searching the sites where $\rho_{\mathrm{air}} + \rho_{\mathrm{wat}}$ is less than a threshold that varies between 1.5 and 1.8 depending on the geometry of the phases distribution.

Once the velocity field at equilibrium is calculated and once the corresponding interfaces positions are mapped, the potential is computed following the equations described in Section 2.3. The potential keeps the constant values $\psi = \zeta_M$ and $\psi = \zeta_I$ at the sites

representing the rock matrix and the air–water interface respectively. The convergence of the potential is assessed thanks to the EK coefficient value, which is obtained by calculating the electrical field. The local electrical field is defined as

$$\boldsymbol{E}(\boldsymbol{x}, t) = -\frac{\rho_e(\boldsymbol{x}, t)u(\boldsymbol{x}, t)c_V}{\sigma_f}. \tag{26}$$

where σ_f is the fluid conductivity. A common expression for σ_f is

$$\sigma_f = \sum_i^n (ez_i)^2 b_i C_i^\infty \tag{27}$$

where $b_i = \frac{1}{6\pi\eta R_i}$ is the mobility of the species i, and R_i its effective ionic radius. It could be noted that the use of eq. (27) to compute eq. (26) amounts to consider that there is no variation of σ_f within the medium. The influence of the local variations of σ_f on the EK coefficient has been assessed in the previous study (Fiorentino *et al.* 2016), and is small for $|\zeta|$ values less than ∼25 mV.

The physical size of the medium must fulfil the condition $2R/d > 120$ so that the diffuse layer's thickness can be considered as negligible compared to the channel's diameter. The number of nodes describing the potential in the direction perpendicular to the flow is then $ny_P = \frac{2R}{d}\frac{d}{dx_P} = 7200$ with $d/dx_P = 60$, which is a lot more than the number of nodes required to simulate the fluid velocity. The velocity used in eq. (26) is thus transposed from the grid used for the velocity computation to the grid used for the potential computation by bilinear interpolation. During this procedure, the position of the zero velocity must be assessed. Indeed, the bounce back condition applied on the solid sites makes the effective position of the wall, where the flow is zero, shift half way between the solid site and the first neighbouring fluid site. The position of the zero velocity is linearly interpolated with the two first neighbouring nodes of the hydric grid.

The macroscopic potential δV is obtained by averaging E over the whole medium. The simulated EK coefficient is obtained using the definition of eq. (1), with the δP that was used to simulate the flow in the preliminary stage. This computation is considered as stabilized when the relative change between two EK coefficients is less than a value ϵ which is small (see next sections). The water saturation S_w is calculated by dividing the number of sites containing water at the end of the simulation by the total number of sites constituting the pore space. The sites representing the air–water interface are excluded from the computations of S_w and EK coefficient because of the non-physical value of the velocity at this place (see Section 2.2).

3 VALIDATION OF THE PROCEDURE

3.1 Validation of the Young-Laplace Law

The validation of the Young-Laplace law is checked so as to verify that the Shan-Chen model is correctly implemented. The domain is initialized with a bubble at rest. A periodic boundary condition is applied to all sides of the lattice, which means that everything that flows out through one side is reinjected at the opposite side. The pressure at the position $\boldsymbol{x}$ can be determined using (Huang *et al.* 2007)

$$P^{\text{ad}}(\boldsymbol{x}) = [\rho_\lambda(\boldsymbol{x}) + \rho_{\bar{\lambda}}(\boldsymbol{x})]/3 + G^{\text{coh}}\rho_\lambda(\boldsymbol{x})\rho_{\bar{\lambda}}(\boldsymbol{x})/3 \tag{28}$$

where P^{ad} is the adimensional pressure in mu H^{-1} ts^{-2} and ρ is the density in mu lu^{-2} H^{-1} with H the out of plane thickness of the system represented by the 2-D flow. The pressure difference between inside and outside the bubble at rest is related to the surface tension γ between the fluids through the Young-Laplace law:

$$\left[P^{\text{ad}}(\boldsymbol{x}_{\text{inside}}) - P^{\text{ad}}(\boldsymbol{x}_{\text{outside}})\right] = \gamma/r_B \tag{29}$$

with r_B the radius of the bubble at equilibrium.

The initial size of the bubble radius must be chosen carefully due to the phenomenon of bubble shrinkage. The bubble shrinkage is a spontaneous non-physical density collapse of the droplet due to the diffusive nature of the fluid interfaces. This artefact was examined numerically and analytically by Zheng *et al.* (2014), who showed that there is a critical radius below which the bubble shrinks until a complete vanishing. This critical radius depends on two parameters that are the ratio of the interface thickness on the radius of the initial bubble, and the ratio of the volume of the computational domain on the volume of the initial droplet. Both of them must be small. To avoid the density shift (bubble shrinkage), the relative importance of the interface thickness compared to the bubble radius must be small, and the relative importance of the bubble volume must not be too low compared to the total volume of the domain. On the other hand, if the droplet is very large, its interface can interfere with itself through the periodic condition at the boundaries, and break the bubble geometry.

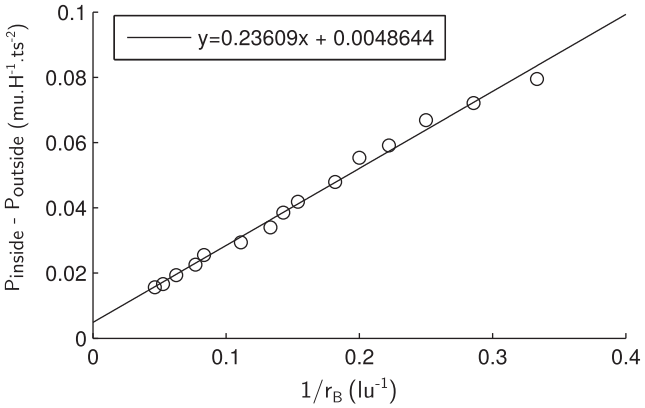

Figure 1. Pressure difference between inside and outside the bubble as a function of $1/r_B$. The adimensional surface tension amounts to $\gamma = 0.236$ mu lu H^{-1} ts^{-2}.

Fig. 1 shows the pressure difference between inside and outside the bubble at rest as a function of $1/r_B$. The domain is a square lattice of side 1.16×10^{-6} m discretized with $nx_V = ny_V = 50$. The medium is initialized such as $\rho_\lambda = \rho_0$ and $\rho_{\bar{\lambda}} = 0$ inside the bubble and $\rho_\lambda = 0$ and $\rho_{\bar{\lambda}} = \rho_0$ outside. The thickness of the interface is fixed by the parameter G^{coh} which controls the surface tension. Huang *et al.* (2007) report that a good compromise between stability and interface thickness is found for $1.6 \leq \rho_0 G^{\text{coh}} \leq 2.0$. The interparticle force is set such as $G^{\text{coh}}\rho_0 = 2$ with $\rho_0 = 2$. The tested bubble sizes range from the critical radius described above until the radius at which the bubble starts to interact through the boundaries. According to Sukop & Thorne Jr (2006), the low resolution of the domain increases the interface thickness and complicates the question of where to measure the densities of each fluid in the vicinity of the interface. This problem yields a non-zero plot intercept of the order of 0.005, which remains acceptable compared to value of 0.001 they obtain for a 200 × 200 domain. The linear trend confirms the ability of the code to reproduce the Young-Laplace law.

In these simulations, the two fluids have the same density and the same viscosity fixed by $\tau = 1$. The surface tension is measured to be $\gamma = 0.236$ mu lu H^{-1} ts^{-2}, which corresponds to a physical value of 0.360 N m^{-1} using H $= dx$. This value is greater than the real air–water surface tension of 0.072 N m^{-1} and is barely tunable, because it is not possible, with the Shan-Chen method, to adjust the surface tension independently from the density and viscosity ratios (Ahrenholz *et al.* 2008). The consequences of a surface tension that is different from the air–water one is discussed later in Section 4.3.

3.2 Flows in parallel

The procedure is validated by calculating an analytical solution when both phases flow in parallel. Air occupies a corridor at the centre of the capillary and water flows on either side between the air and the rock walls.

3.2.1 Analytical solution

The geometry of parallel flows is sufficiently simple to compute an analytical expression of the EK coefficient as a function of S_w. The charge density of the electrolyte is given by eq. (23). The species concentrations obey a Boltzmann distribution given by eq. (24). With the assumption that the fluids have the same dynamic viscosities, the velocity of the electrolyte should follow a Poiseuille profile

$$v(\chi) = \frac{1}{2\eta}\frac{\delta P}{L}(\chi(2R-\chi)) \tag{30}$$

with χ the distance from the rock surface. The potential gradient along the capillary is expressed as

$$\frac{\delta V}{L} = -\langle E\rangle = -\frac{\langle v\rho_e\rangle}{\sigma_f} \tag{31}$$

where σ_f is the electrolyte conductivity defined by eq. (27). This gives, with the definition of $C_{\rm EK}$ and using eqs (23) and (30):

$$C_{\rm EK} = \frac{\delta V}{\delta P} = \frac{e^2C^\infty}{\eta k_{\rm B}T\sigma_f}\mathcal{I} \tag{32}$$

where

$$\mathcal{I} = \frac{1}{2R}\int_0^{2R}\chi(2R-\chi)\psi(\chi)\mathrm{d}\chi. \tag{33}$$

The Debye-Hückel approximation (Pride 1994) allows to express the potential as

$$\psi(\chi) = \zeta e^{-\frac{\chi}{d}} \tag{34}$$

where d is a characteristic lengthscale termed the Debye length which measures the thickness of the diffuse layer:

$$\frac{1}{d^2} = \sum_i^n \frac{(ez_i)^2C_i^\infty}{\varepsilon_0\varepsilon_r k_{\rm B}T} \tag{35}$$

with $\varepsilon_0 = 8.8531\,10^{-12}$ F m^{-1} the vacuum permittivity and ε_r the relative permittivity of water, equal to 80.1 at 20 °C for a salinity <0.1 mol L^{-1}. Using eq. (34), $\mathcal{I}$ can be split into two contributions, the contribution from the potential of the capillary walls denoted $\mathcal{I}_{\rm rock}$

$$\mathcal{I}_{\rm rock} = \frac{\zeta_M}{2R}\int_0^{2R}\chi(2R-\chi)[e^{-\frac{\chi}{d}} + e^{-\frac{-(2R-\chi)}{d}}]\mathrm{d}\chi \tag{36}$$

and the contribution from the potential of the fluid–fluid interfaces denoted $\mathcal{I}_{\rm flow}$

$$\begin{aligned}\mathcal{I}_{\rm flow} = {}& \frac{\zeta_I}{2R}\int_0^{h_1}\chi(2R-\chi)[e^{-\frac{(h_1-\chi)}{d}} + e^{-\frac{(h_2-\chi)}{d}}]\mathrm{d}\chi\\ &+ \frac{\zeta_I}{2R}\int_{h_1}^{h_2}\chi(2R-\chi)[e^{-\frac{(\chi-h_1)}{d}} + e^{-\frac{(h_2-\chi)}{d}}]\mathrm{d}\chi\\ &+ \frac{\zeta_I}{2R}\int_{h_2}^{2R}\chi(2R-\chi)[e^{-\frac{(\chi-h_1)}{d}} + e^{-\frac{(\chi-h_2)}{d}}]\mathrm{d}\chi,\end{aligned} \tag{37}$$

where h_1 and h_2 are the positions of the fluid–fluid interfaces. With the assumption that these interfaces are symmetrical with respect to the central axis parallel to the flow, they can be rewritten as a function of the water saturation S_w like

$$h_1 = RS_w \quad \text{and} \quad h_2 = 2R(1 - S_w/2) \tag{38}$$

where S_w varies between 0 (no water) and 1 (no air). By remarking that the potential is non-zero only in the very close vicinity of the interface and that the velocity in this area can be approximated to the velocity of the interface, eq. (37) simplifies to

$$\mathcal{I}_{\rm flow} = \alpha\zeta_I\frac{dh_1(2R-h_1)}{2R} = \alpha\zeta_I\frac{dR^2}{2R}S_w(2-S_w) \tag{39}$$

with $\alpha = 4$. By remarking that the velocity of the fluid-fluid interface is much more important than the velocity near the rock, the contribution $\mathcal{I}_{\rm rock}$ can be neglected and $C_{\rm EK}$ can be approximated to

$$C_{\rm EK} = \alpha\frac{e^2C^\infty\zeta_I}{2\eta k_{\rm B}T\sigma_f}dRS_w(2-S_w). \tag{40}$$

3.2.2 Simulations

The medium is initialized by setting the air phase at the centre of the capillary and the water phase on either side of the corridor formed by the air. Starting from now and until the end of this paper, the density is initialized such as $\rho_{\rm air} = \rho_0$ and $\rho_{\rm wat} = 0$ in the phase representing air, $\rho_{\rm air} = 0$ and $\rho_{\rm wat} = \rho_0$ in the phase representing water, and $\rho_{\rm air} = \rho_{\rm wat} = \rho_0/2$ at the sites representing the rock, meaning that the total density is initialized to $\rho_{\rm air} + \rho_{\rm wat} = \rho_0$ in the whole medium. $G^{\rm coh}$ is fixed such as $G^{\rm coh}\rho_0 = 2$ with $\rho_0 = 2$. A periodic condition is applied at the boundaries perpendicular to the flow, and a bounce back condition is applied at the boundaries parallel to flow, meaning that all the particles that reach these boundaries are sent back in the opposite direction.

The velocity is computed until the relative change between 100 computations is less than 10^{-9}. The convergence is reached after ∼100 000 ts. The concentration of the electrolyte is fixed at 10^{-3} mol L, and the channel's diameter is 1.16×10^{-6} m so that the criterion $2R/d > 120$ is verified. Both phases have the viscosity $\nu^{ad} = 0.1666$ giving the same relaxation time $\tau = 1$. The size of the velocity grid is $ny_V = 100$, $nx_V = 10$. The lattice speed is $c_V = 514$ m s^{-1}. The dx_P of the potential grid must fulfil the condition $d/dx_P \sim 60$, giving $ny_P = 7200$ and $nx_P = 655$. The computation of the potential stops when the relative change between 10 computations of $C_{\rm EK}$ is less than 10^{-8}. The convergence of the potential is achieved after ∼130 000 iterations, which takes 2 hr, parallelized on a 16 cores computer. The imposed pressure difference δP is 6.7×10^4 Pa. The potentials of the air–water and fluid-rock interfaces ζ_I and ζ_M are both set to −20 mV.

In Fig. 2(a), the simulated velocity is compared to the theoretical Poiseuille profile. The peaks located at the interfaces positions h_1

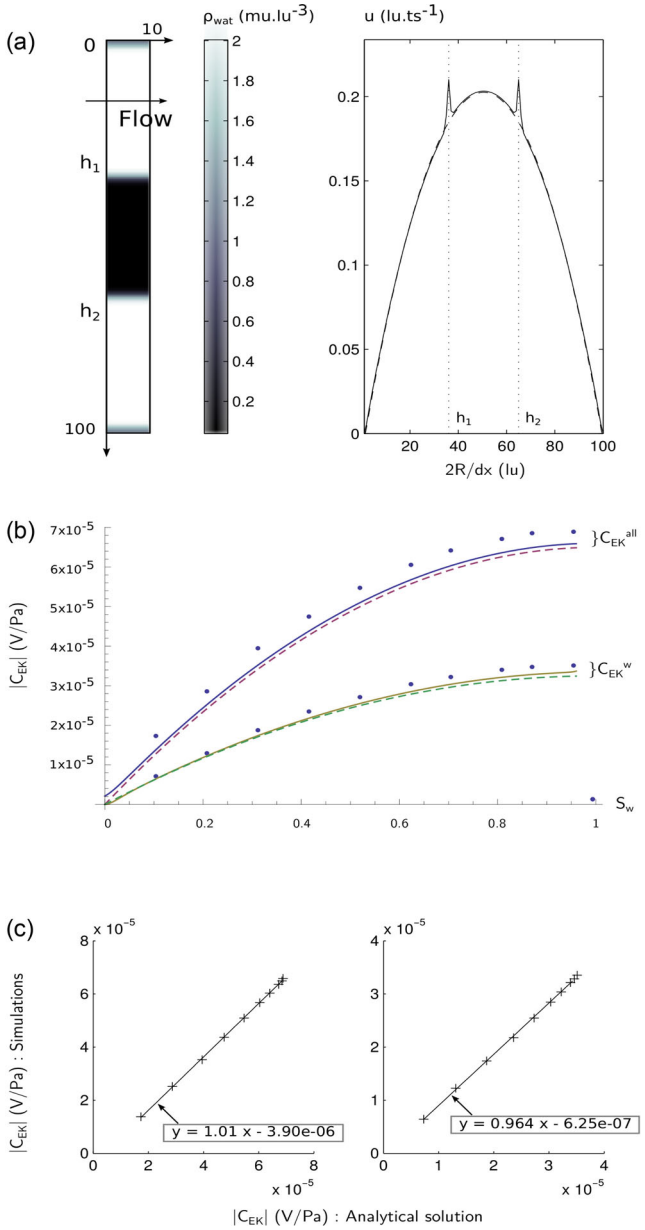

Figure 2. (a) Left: density of the water phase in a lattice 10 × 100. Right: simulated velocity profile (solid line) and theoretical Poiseuille profile (dashed line). The spurious velocities can be observed at the interfaces placed at h_1 and h_2. The velocity is in lattice units. The physical velocity is obtained using $c_V = 513$ m s^{-1}. (b) EK coefficient as a function of S_w: comparison between eq. (32) (solid lines), eq. (40) (dashed lines) and the simulations (dots). For the comparison with $C^w_{\rm EK}$, eq. (32) is adapted by removing the second integral in eq. (37) and eq. (40) is obtained using $\alpha = 2$. (c) Simulated EK coefficient against analytical calculation: $C^{\rm all}_{\rm EK}$ on the left, $C^w_{\rm EK}$ on the right.

and h_2 are the so-called spurious currents, whose magnitude can be obtained by subtracting the Poiseuille velocity to the simulations. This magnitude varies between 0.009 lu ts^{-1} and 0.027 lu ts^{-1} from the lowest to the highest tested S_w. This is below the value of 0.059 lu ts^{-1} obtained by Hou *et al.* (1997) for a rounded bubble.

Two EK coefficients are calculated: an EK coefficient denoted $C^{all}_{\rm EK}$ which involves all the sites of the domain, and another one, denoted $C^w_{\rm EK}$, which excludes the sites belonging to the air phase, at the centre of the capillary. Only the second one has a physical meaning, since the first one would be the result for conductive air. The sites containing air are caught by tracking the sites where $\rho_{\rm air} > 1$. As mentioned in Section 2.4, the lattice sites located at the interface are excluded from the computation of the EK coefficient so as to remove, at least partly, the artefact caused by the spurious velocities.

3.2.3 *Comparison*

Fig. 2(b) shows the comparison between eq. (32) and the simulated EK coefficient. Fig. 2(c) shows a crossplot of the simulations versus the analytical solution. The algorithm provides reliable results, as shown by the unitary slope. The small difference observable in Fig. 2(b) is attributed to the presence of the spurious velocities. These spurious currents slightly increase the EK coefficient, but do not modify its behaviour. The increasing trend of $C_{\rm EK}$ with increasing S_w is triggered by the positive charge excess associated to the fluid-fluid interfaces. This positive charge excess is magnified by the flow velocity. The higher S_w, the closer to the channel's centre the positive charge excess, the higher the velocity, and the higher the enhancement. The EK coefficient is here a continuous, increasing function of S_w, until the medium is completely filled with water. When $S_w = 1$, the fluid-fluid interfaces do not exist anymore, and the EK coefficient collapses to the value determined by the Helmholtz–Smoluchowski (HS) equation which gives the EK coefficient at full water saturation:

$$C_{\rm EK} = \frac{\varepsilon_0 \varepsilon_r \zeta_M}{\eta \sigma_f}. \tag{41}$$

As it could be expected, the values of $C^w_{\rm EK}$ represent the half of the values of $C^{all}_{\rm EK}$. This relies on the fact that the contribution of the charge density near the fluid-fluid interface completely overwhelms the contribution of the capillary walls, due to the increase of the velocity approaching the centre of the channel. Removing the inner part of the corridor is like removing one half of the profile close to the interface, where the potential is not negligible; the rest does not contribute to the electrokinetic coupling. Starting from now, the EK coefficient will refer to $C^w_{\rm EK}$ which corresponds to an air–water system, the air phase being an electrical insulator that does not support any conduction current. The good agreement between eqs (32) and (40) plotted in dashed line in Fig. 2 validates again that the contribution of the fluid-fluid interface overwhelms the contribution of the fluid-rock area, since it is one of the hypothesis used in the derivation of eq. (40).

It should be noted that the example of parallel flows could not really occur at very high S_w due to the Rayleigh Plateau instability. It is essentially a useful configuration for comparison with an analytical solution and validation of the code. In reality, a thin corridor of air would be split into a multiple bubbles configuration, which will be analysed later in this paper.

3.3 Choice of the ζ potential

For an NaCl electrolyte at pH = 7, the literature reports potential values of the air–water interface comprised between −20 and −40 mV (Yang *et al.* 2001a; Takahashi 2005; Creux *et al.* 2007; Leroy *et al.* 2012). The ζ_M potential of the fluid-rock interface is generally described as a decreasing function of the electrolyte concentration (e.g. Kirby & Hasselbrink 2004). Some studies suggest it

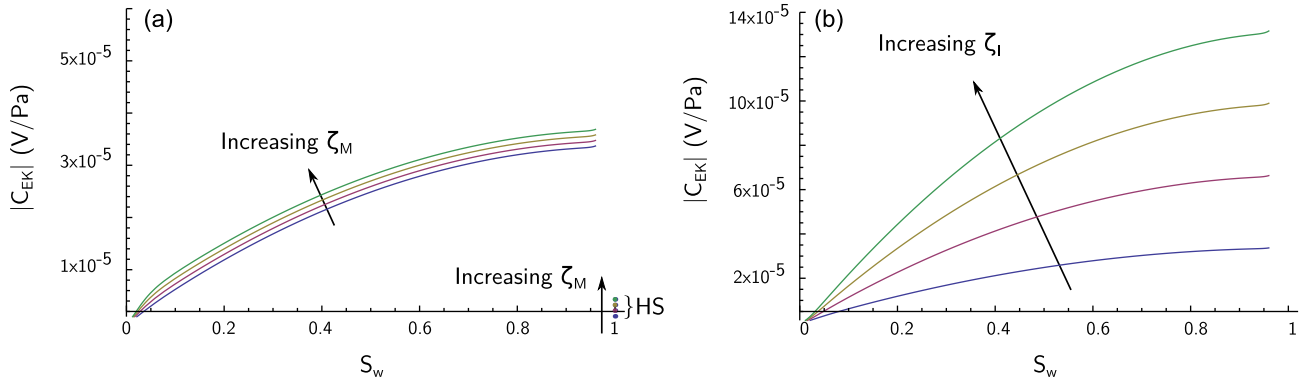

Figure 3. C_{EK} as a function of S_w. The dots represent the HS equation (EK coefficient at the saturated state). (a) Computation with $\zeta_I = -20$ mV and $\zeta_M = \{-20, -40, -60, -80\}$ mV. (b) Computation with $\zeta_I = \{-20, -40, -60, -80\}$ mV and $\zeta_M = -20$ mV.

can be constant of about −20 mV on sands and sandstones (Jouniaux & Ishido 2012) or suggest that this salinity-dependence might be blurred considering complex porous networks as encountered in realistic rocks (Lorne *et al.* 1999b; Fiorentino *et al.* 2016).

Fig. 3(a) shows eq. (32) computed for $\zeta_I = -20$ mV and $\zeta_M = \{-20, -40, -60, -80\}$ mV. The dots represent the HS equation. We can observe an increase of the EK coefficient with increasing ζ_M, but this increase remains low compared to the general increase observed from full to partial water saturation. A contrario, when ζ_M is fixed, the variations of ζ_I impact the EK coefficient in a quasi-proportional manner (Fig. 3b). This illustrates again that the SP response is dominated by the contribution of the gas-water interface, whose associated charge density is magnified by the local velocity of the fluid. The value of ζ_I appears to be a key parameter controlling the magnitude of the EK coefficient. The potential of the fluid-rock interface can thus be set arbitrarily, considering the weakness of its impact. For the rest of this study, both ζ_I and ζ_M will keep the value of −20 mV.

4 RESULTS

The behaviour of the EK coefficient is now examined when the non-wetting phase is discontinuous at the scale of the capillary. We recall that the simulations of this work are 2-D simulations. For a monophasic electrolyte, the correspondence between these simulations and a 3-D analytical solution assuming an axisymmetric geometry was shown to be valid (Fiorentino *et al.* 2016). This question is a bit more complex in biphasic conditions, where the distribution of the non-wetting phase has more degrees of freedom in 3-D than in 2-D. This probably induces a certain variability of the EK coefficient, but we do not think that this modifies the overall process presented in the following study.

4.1 Entrapped bubbles

In this section, we focus on the behaviour of the EK coefficient when bubbles are entrapped in anfractuosities. Different configurations are simulated so as to compute the EK coefficient at several saturations. The resulting systems are presented in Fig. 4. The wetting properties are fixed with $G^{\mathrm{ads}}_{\mathrm{wat}} = 0.3$ and $G^{\mathrm{ads}}_{\mathrm{air}} = -0.2$ ($\cos\theta = -0.5$). The velocity grid is $ny_V = 100$, $nx_V = 150$. The channel's diameter is a bit wider than in Section 3.2.2 so that the narrowest distance between the channel's walls is still $>120d$. The asperities have a 10 lu width, so that 80 lu represent 1.16×10^{-6} m. This gives a channel diameter $2R = 1.45 \times 10^{-6}$ m. With the criterion $d/dx_P \sim 60$, the potential grid is $ny_P = 9024$, $nx_P = 13582$. The viscosity of the fluids is $\nu^{ad} = 0.1666$, giving the lattice velocity $c_V = 411$ m s^{-1}.

The pressure drop along the capillary is 6.29×10^5 Pa, giving the pressure gradient $\|\nabla P\| = 2.9 \times 10^{11}$ Pa m^{-1} with $L = 3R$. This value is not representative of pressure gradients that can be found in realistic geologic media, and is made strong for numerical purposes only. A strong velocity makes the spurious currents less observable, and decreases the shrinkage of the small bubbles. It should be noted however that keeping the same ratio $2R/d$, these simulations could represent an electrolyte with a smaller concentration flowing in a wider channel, giving a lower pressure gradient, and thus a smaller velocity. According to eq. (35), a decrease of the concentration such as $C_2 = (1/\lambda)C_1$ with $\lambda > 0$ would yield an increase of the Debye length $d(C_2) = \sqrt{\lambda} d(C_1)$, equivalent to an increase of the channel's radius $R(C_2) = \sqrt{\lambda} R(C_1)$, giving a velocity increase $v(C_2) = \lambda v(C_2)$ according to eq. (30).

The velocity fields show oscillations that do not completely fade away, so the convergence is assessed over a long period, typically when the relative change between 10 000 computations of the average velocity is less than 10^{-4}, which can take up to 65 800 ts. The convergence of the potential is reached when the relative change between 10 C_{EK} computations is less than 10^{-6}. This is achieved after ∼72 000 ts, which takes between 24 and 28 hr on a 16 cores parallel computer. At the end of the simulation, all the sites belonging to the air phase are zeroed so as to take into account the water phase only, and the electrical field is averaged over the whole space, giving the simulated EK coefficient.

The charge density is averaged over the number of sites belonging to the water phase, and is compared in Fig. 5(a) to the interface area, i.e. the number of lattice sites constituting the gas-water frontier. Both of them are decreasing functions of S_w. The velocity averaged over the whole medium (excluding the sites constituting the interface that are non-physical) is an increasing function of S_w (Fig. 5b). This is consistent with the analysis of Sherwood (2007); Sherwood *et al.* (2013) who showed that for a given pressure gradient, the injection of bubbles modifies the relationship between the total flow rate and the pressure drop. This behaviour corresponds to the decrease of relative permeability with increasing air saturation invoked by the models of Perrier & Morat (2000), Linde *et al.* (2007), Revil *et al.* (2007), Jackson (2008, 2010), Jougnot *et al.* (2012). The EK coefficient (Fig. 5c) exhibits a non-monotonous trend, that results

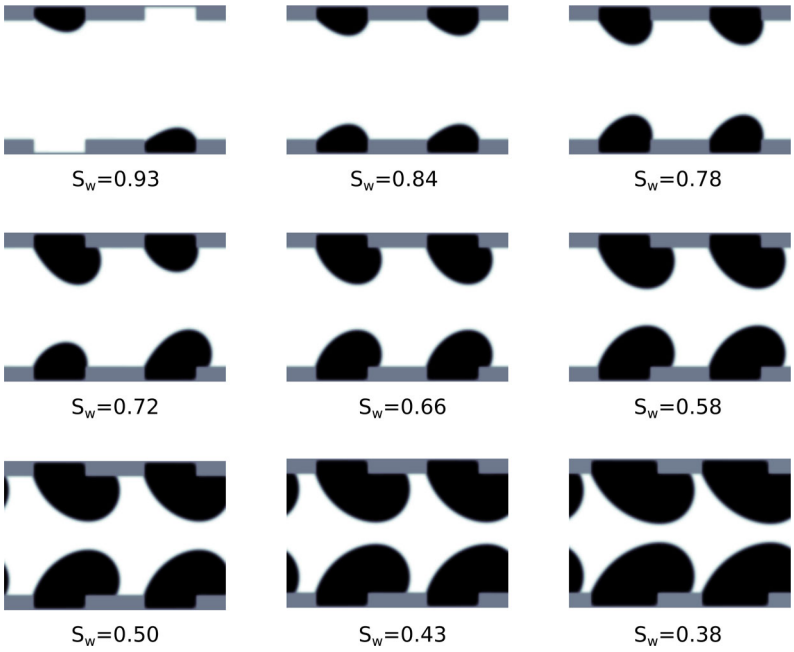

Figure 4. Bubbles trapped in asperities for several saturations. Rock in grey, air in black, water in white.

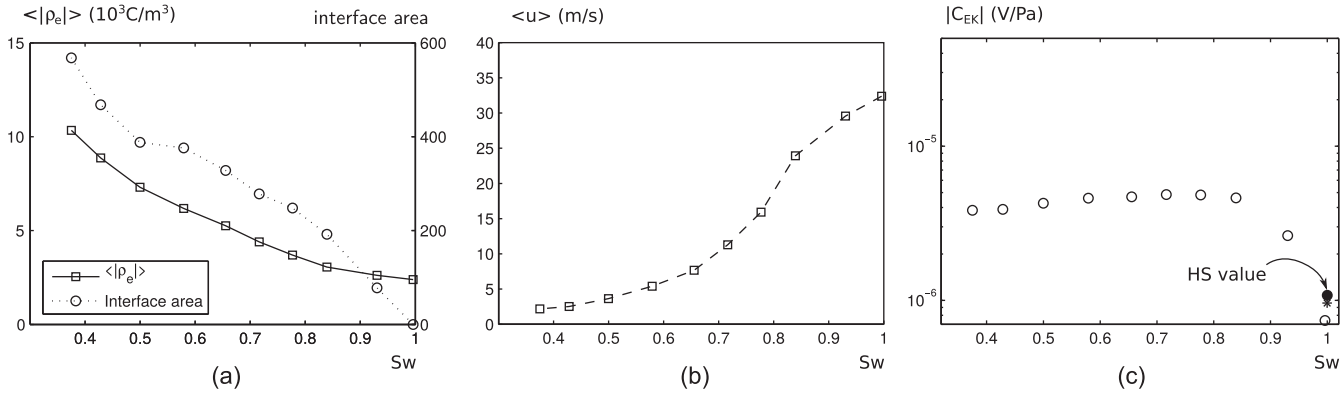

Figure 5. Trapped bubbles configuration (see Fig. 4). (a) Charge density averaged over the number of water sites, and interface area versus S_w. (b) Velocity of the electrolyte averaged over the whole pore space versus S_w. (c) EK coefficient versus S_w. The solid circle is the Helmholtz–Smoluchowski reference, the star is the configuration $S_w = 0.84$ with the bubbles replaced with rock.

from the combination of the decrease of velocity with the increase of total volumic charge density at decreasing S_w.

For any saturation, the EK coefficient is stronger than the value at full saturation given by the HS equation. An increase by a factor four to five can be observed compared to the saturated state. This enhancement is explained by the presence of an excess charge at the gas-water interface, which increases the average charge density. Another reason for that is the fact that when the walls of the capillary harbour bubbles, the velocity of the electrolyte approaching the capillary surface is non zero, due to the continuity of the tangential component of the velocity at the fluid-fluid interface. The velocity in the bubble being non-zero, the velocity at the frontier between air and water is greater than the velocity if the bubble area were made of solid rock. This phenomenon is illustrated by Fig. 6 which shows the velocity field of the configuration $S_w = 0.84$, and the velocity field computed by replacing the air phase with rock. In the presence of bubbles, the average velocity is 24 m s^{-1}, against 21 m s^{-1} in the monophasic situation. The resulting EK coefficient is -9.61×10^{-7} V Pa^{-1} in the single-phase case (denoted by a star in Fig. 5c), and increases to -4.62×10^{-6} V Pa^{-1} in the two-phase situation, for the same average charge density of 3 kC m^{-3}.

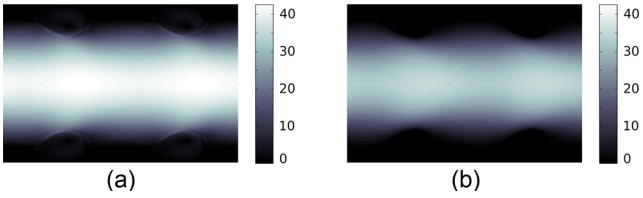

Figure 6. (a) Velocity field in the configuration $S_w = 0.84$ (trapped bubbles, Fig. 4). (b) Velocity field obtained by replacing the bubbles with rock.

As side remark, we can notice that the EK coefficient computed at full water saturation is -7.71×10^{-7} V Pa^{-1}, which is lower than the HS forecast of -1.08×10^{-6} V Pa^{-1}. This shows again (Fiorentino *et al.* (2016), appendix) that the presence of anfractuosities, which breach the smooth capillary assumption on which the HS equation is based, results in a decrease of the magnitude of the EK coefficient.

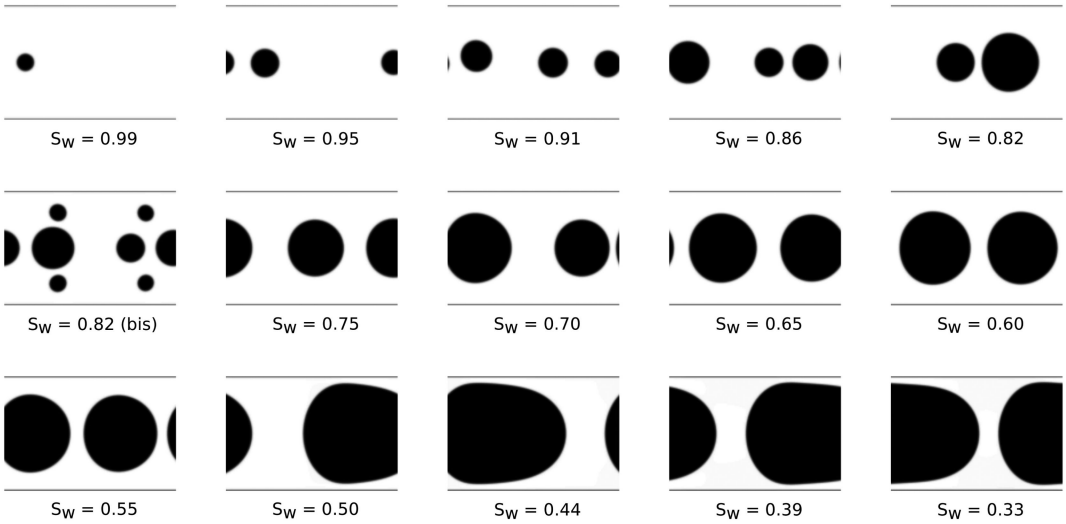

Figure 7. Bubbles flowing at different saturations. Rock in grey, air in black, water in white.

4.2 Flowing bubbles

An air injection is simulated by imposing $\rho_{\text{air}} = \rho_0$ and $\rho_{\text{wat}} = 0$ on a portion of sites, in the centre of the channel for several steps at the beginning of the simulation (e.g. Parmigiani *et al.* 2011). The quantity of air injected in the system is tuned by varying the duration, the position and the period of injection. The injection is made between $t = 5000$ ts and $t = 6200$ ts for the highest S_w, and $t = 25\,000$ ts for the lowest S_w. The resulting systems are presented in Fig. 7. The associated contour line plots of the velocity field are shown in Fig. A1 (see the Appendix). The fact that the bubbles are not created with the same injection time, before the establishment of the steady state explains why the bubbles have different sizes. The configuration 'bis' at $S_w = 0.82$, and later denoted S^*_{82}, has an interface area 75 per cent greater than the two-bubble configuration at the same saturation. It allows to assess the impact of the fractioning of the non-wetting phase.

The wetting properties are set using $G^{\text{ads}}_{\text{wat}} = 0.5$ and $G^{\text{ads}}_{\text{air}} = -0.4$ ($\cos\theta = -0.9$), so that there is a strong repulsion between the phase representing air and the capillary walls. The channel's diameter is 1.16×10^{-6} m. The dimensions of the velocity grid are $ny_V = 100$, $nx_V = 150$. The convergence of the flow is reached when the relative change of the mean velocity is less than 10^{-5} over 100 ts, which can take up to 50 600 ts. The dimensions of the potential grid are $ny_P = 7200$, $nx_P = 10\,836$. Both fluids have the viscosity $\nu^{ad} = 0.4$. The lattice velocity c_V is 214 m s^{-1}. The convergence of the potential is achieved when the relative change between 10 C_{EK} computations is less than 10^{-6}. The simulations stop after ~72 000 ts, which represents between 15 and 19 hr of calculation on a 16 cores parallel computer. The same pressure gradient as the trapped bubbles configuration is applied, which yields a pressure drop of 5.03×10^5 Pa along the capillary using $L = 3R$.

The assumption that the charge density scales with the inverse of S_w implies that there is no positive charge excess associated to the gas-water interface. For comparison, the corresponding situation is simulated by setting $\zeta_I = 0$ V in the computation of the potential and using the same flow configurations. The resulting average charge density is plotted together with the average charge density of the simulations with $\zeta_I = -20$ mV in Fig. 8(a). A significant divergence can be observed with decreasing S_w, with a factor close to 2 at the lowest tested saturation. The interface area shows a good correlation with the average charge density computed with a non-zero ζ_I: it increases with decreasing S_w and drops when the bubbles merge.

Similarly to what was observed in the entrapped bubbles case, the average velocity of the flow decreases with decreasing S_w (Fig. 8b). The EK coefficient shows a non-monotonous behaviour, with an enhancement up to a factor 30 compared to the saturated state (Fig. 8c, circles). The EK coefficients computed with $\zeta_I = 0$ V (crosses) are shown for comparison: in that case, the EK coefficient is constant or slightly decreasing with decreasing S_w.

The configuration S^*_{82} yields a charge density increase of 41 per cent and a velocity decrease of 7 per cent compared to the two-bubbles configuration at the same saturation. The corresponding EK coefficient is represented by a star in Fig. 8(c) and amounts to -3.72×10^{-5} V Pa^{-1} against -2.38×10^{-5} V Pa^{-1} for the two-bubbles case, which is a significant difference. For a given saturation, increasing the fractioning of the gas phase results in an increase of the EK coefficient, which illustrates again the correlation between charge density and interface area.

4.3 Influence of the pressure gradient

The expression used to validate the simulations in a situation where the phases flow in parallel (eq. 32), is independent of the pressure gradient. However, it could be expected that when the non-wetting phase forms discontinuous bubbles, the pressure gradient is able to influence the EK coefficient.

The configuration $S_w = 0.91$ in Fig. 7 is computed with a pressure gradient $\|\nabla P\| = 1.2 \times 10^{12}$ Pa m^{-1}, which is 4 times larger than the pressure gradient $\|\nabla P\| = 2.9 \times 10^{11}$ Pa m^{-1} that was used in Section 4.2. The simulated EK coefficients are -2.58×10^{-5} V Pa^{-1} in the first case and -2.60×10^{-5} V Pa^{-1} in the latter. The slight discrepancy (less than 1 per cent) can be attributed to the difference in the bubbles spreading, and appears negligible.

In the trapped bubbles configuration $S_w = 0.66$ presented in Section 4.1, the EK coefficient amounts to -4.69×10^{-6} V Pa^{-1} using the pressure gradient $\|\nabla P\| = 2.9 \times 10^{11}$ Pa m^{-1}. By imposing a higher gradient such as 6.0×10^{11} Pa m^{-1}, it is possible to observe

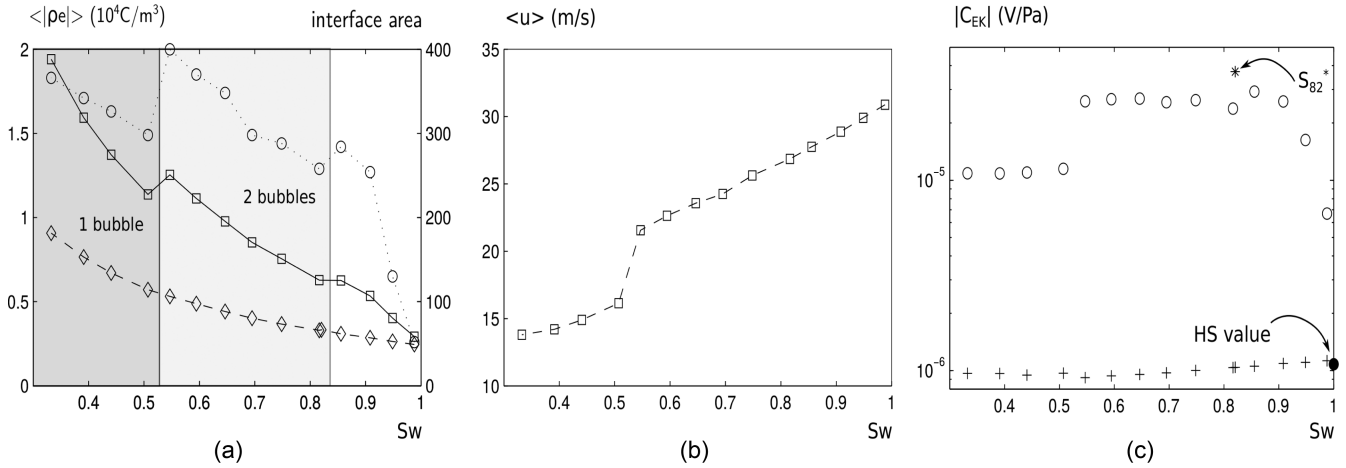

Figure 8. Flowing bubbles configuration (see Fig. 7). (a) Charge density in the water computed for $\zeta_I = 0$ V (diamonds) and $\zeta_I = -20$ mV (squares) versus S_w, with $\zeta_M = -20$ mV in both cases. Interface area (circles) versus S_w. The simulations in the dark grey box involve a single bubble, the simulations in the light grey box involve two bubbles, the simulations in the white box involve bubbles that are sufficiently small to avoid merging. (b) Average flow velocity versus S_w. (c) EK coefficient versus S_w for $\zeta_I = -20$ mV (open circles) and $\zeta_I = 0$ V (crosses). The configuration S^*_{82} (star) allows to assess the impact of the fractioning of the non-wetting phase. The solid circle denotes the Helmholtz–Smoluchowski value.

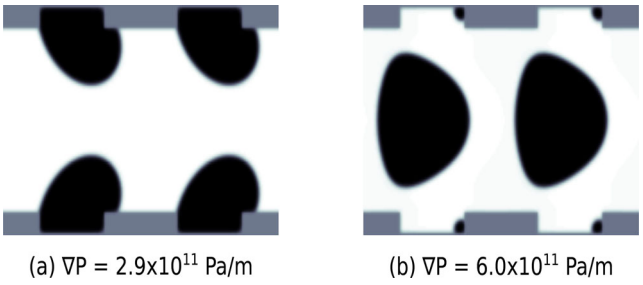

Figure 9. (a) View of the medium with entrapped bubbles at saturation $S_w = 0.66$ and $\|\nabla P\| = 2.9 \times 10^{11}$ Pa m^{-1}. (b) View of the medium starting with the same initial conditions with $\|\nabla P\| = 6.0 \times 10^{11}$ Pa m^{-1}.

the release of the entrapped bubbles. The opposite bubbles join the main flow, merge and switch to a flowing configuration (see Fig. 9). Once the equilibrium state is reached, the EK coefficient jumps to -2.63×10^{-5} V Pa^{-1}, which is an increase of a factor 6.

The difference between the EK coefficient value obtained after the merging of the bubbles and the EK coefficient obtained with $\|\nabla P\| = 2.9 \times 10^{11}$ Pa m^{-1} in Section 4.2 at a similar saturation (Fig. 7, $S_w = 0.65$) is of the order of 2 per cent.

These results mean that increasing the pressure gradient allows to observe a discontinuity between the two regimes (entrapped and flowing bubbles), but for a given situation, the value of the pressure gradient does not modify the SP response. Using a high pressure gradient allows to switch from a trapped configuration to a flowing configuration, and thus to generate an enhancement of the EK coefficient, but for a given stable configuration, the pressure gradient does not influence the SP response. In other words, when the flow velocity decreases because the pressure gradient is modified, the change of macroscopic potential difference is proportional to the change of pressure gradient. According to eq. (1), this change is cancelled due to the division by δP, and the EK coefficient remains unchanged. Some small fluctuations can come from the repartition of the bubbles, or their deformation if the velocity is very high. If the flow velocity decreases at constant pressure gradient, then the decrease of δV will not be compensated by δP, and the EK coefficient will decrease. In that case, the decrease of the flow velocity is due to the increasing presence of the non-wetting phase which decreases the relative permeability of the medium. The dynamic state of the non-wetting phase has a significant impact on the EK coefficient notably because it is related to the relative permeability. The two regimes corresponding to the flowing and entrapped bubbles represent two different levels of relative permeability, and this is one of the reasons why the switching from one regime to the other has such spectacular effects.

By balancing the pressure gradient exercised along the entrapped bubble to the capillary pressure, we can express the critical pressure gradient $\|\nabla P\|^{\text{crit}}$ needed to overcome the surface force which maintains the bubble on the rock capillary as

$$\|\nabla P\|^{\text{crit}} = \frac{\gamma}{r_B^2}. \tag{42}$$

With $r_B = 35$ lu, $dx_V = 1.46 \times 10^{-8}$ m and the γ value estimated in Section 3.1, the calculation gives $\|\nabla P\|^{\text{crit}} = 1.37 \times 10^{12}$ Pa m^{-1}. This remains consistent with the $\|\nabla P\|^{\text{crit}}$ observed in the simulations, comprised in the range $3–6 \times 10^{11}$ Pa m^{-1}, since eq. (42) does not take into account the geometry of the asperity and the contact angle properties. For the present case, the repulsion between the air phase and the solid phase contributes to the decrease of $\|\nabla P\|^{\text{crit}}$. In this model, the value of $\|\nabla P\|^{\text{crit}}$ is the only way the surface tension between the two fluids influences the general mechanism.

Another question related to the pressure gradient is whether the flow is still in the laminar regime despite the strong imposed pressure drop. This feature is quantified thanks to the Reynold's number defined as

$$Re = \frac{Ul}{\nu} \tag{43}$$

where U is a characteristic velocity chosen here as the maximum velocity, and where l is a characteristic length of the medium, typically the pore diameter. This question matters since according to the study of Watanabe & Katagishi (2006), the EK coefficient begins to deviate from the HS equation at Reynold's number >3. The Reynold's numbers of the present simulations are much higher. However, the mechanism proposed by Watanabe & Katagishi (2006) to explain this deviation, based on the work of Lorne *et al.* (1999a), is the occurrence of counter-flows in the crevices of the irregularly shaped

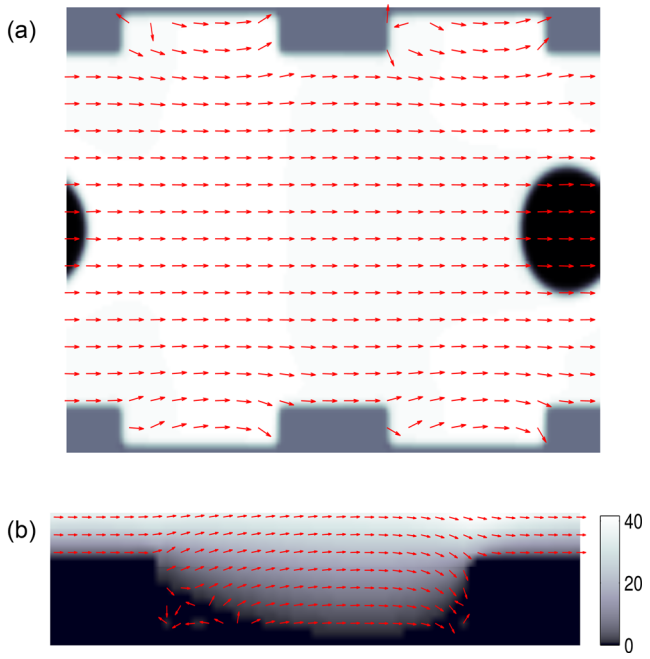

Figure 10. Simulation in a channel with asperities. The parameters are $2R = 1.16 \times 10^{-6}$ m, $\|\nabla P\| = 1.2 \times 10^{12}$ Pa m^{-1}. The maximum velocity is $U = 131$ m s^{-1}, giving Re = 152. (a) Velocity directions (red arrows). Rock in grey, air in black, water in white. (b) Velocity directions superimposed on the velocity norm (m s^{-1}), zoom on an asperity.

channel, leading to a decrease of the EK coefficient when the flow is fast. Most of the present simulations take place in a smooth capillary which is not prone to generate such counter-flows. When the channel is irregularly shaped we can observe some fluctuations of the velocity directions in the anfractuosities (see Fig. 10a). However, these fluctuations correspond to very small velocity amplitudes (less than 1 m s^{-1}, see Fig. 10b) which can be safely neglected compared to the velocity of the main flow (maximum velocity $U = 131$ m s^{-1}). If they were not, they would mask a further increase of the EK coefficient.

5 DISCUSSION

In this paper, the influence of a non-zero potential at the gas-water interface has been investigated. The results show that this contribution is a key component of the EK response in unsaturated conditions. The fluid–gas interfaces generate an enhancement of the EK coefficient not only because they increase the charge density, but also because they are placed away from the rock surface, where the related positive charge excess is multiplied by a large velocity. The distribution of the air phase greatly affects the magnitude of the streaming potential enhancement. It can be observed in Fig. 11 that the configuration of parallel flows is a kind of maximum envelope of the EK coefficient in unsaturated conditions, because in this case, the interface is located in the area that maximizes the velocity multiplying its associated charge density. When the air takes the form of bubbles, the flow velocity is slowed, which results, combined with the increase of charge density with increasing air saturation, in a non-monotonous behaviour of the EK coefficient. At high S_w, C_{EK} increases compared to the saturated state because of the apparition of the polarized air–water interfaces. When S_w decreases, the related positive charge excess increases, and so does the EK coefficient. At high S_w, the velocity decrease remains low

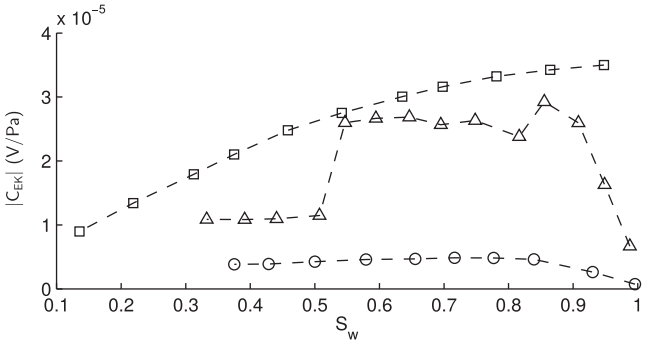

Figure 11. Comparison of the EK coefficients simulated with $\zeta_M = \zeta_I = -20$ mV for the three types of air distribution: flow in parallel (squares), bubbles flowing (triangles), entrapped bubbles (circles).

and does not prevent C_{EK} from increasing. Below a critical S_w, the velocity decrease overcomes the charge density increase, leading to a constant (Fig. 5c) or decreasing (Fig. 8c) EK coefficient. The velocity decrease reflects the decrease of relative permeability at low S_w. When the air is entrapped in the crevices of the porous network, the enhancement is lower, because the interface is placed in areas where the fluid velocity is lower.

A weakness of this model could be the use of a unitary viscosity contrast between the air and the water phase. We think nonetheless that it does not change the main conclusions of this work. In the case of the bubbles flowing, the deformation of the bubbles at $S_w < 0.5$ (see Fig. 7) is quite similar to what can be observed for real air bubbles propagating at high speed. The velocity profile inside the bubble is roughly homogeneous (see Fig. 12), meaning that the viscosity of the phase representing air is not a sensitive parameter. Considering the trapped bubble case, we know from Fig. 6 that the convection movement described by the air phase in the bubble accelerates the water flow compared to the solid case. This convection cell turns slowerly than if it were real air, because real air is less viscous than the viscosity used in these simulations. Consequently, a real air bubble would even more increase the velocity of the electrolyte, which would further increase the EK coefficient value, and thus reinforce these results.

The mechanisms creating the negative potential of the air–water interface being not thoroughly understood, an assumption that is implicitly made in this paper is that the negative charges causing the ζ_I potential are placed in the air. In monophasic conditions, the negative potential of the rock matrix creates a positive charge excess that creates an electrical current when these positive ions are dragged with the flow; this current is counterbalanced by the conduction current, but is not counteracted by the negative charges causing ζ_M, because these charges stand still at the rock surface. In multiphase conditions, we made the hypothesis that the negative charges are placed in the air phase and do not contribute to the calculation of C_{EK}, since the potential difference δV is measured in the water. However, if these negative charges were in the water, they should be taken into account in the calculation of the local electric charge density. This would not impact the configuration of trapped bubbles, because in that case the air–water interface does not move, and the negative charges adsorbed at this interface would not create any current. In contrast, the flowing bubbles configuration would be very impacted, because in that case the interface is flowing, and the negative charges moving with the interface would create a countercurrent balancing the current associated to the positive charge excess. The contribution of the air-water interface to δV would only come from the velocity difference between the negative

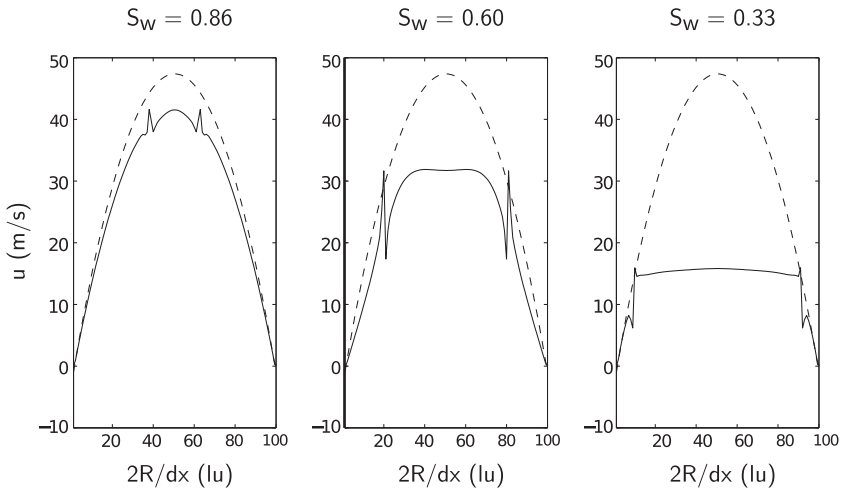

Figure 12. Velocity profiles in m s^{-1} of the configurations $S_w = 0.86$, 0.60 and 0.33 (see Fig. 7). Cross-sections at 1/5 from the left of the capillary. Theoretical Poiseuille profile in dashed line.

charges creating ζ_I and the positive charges screening ζ_I, which is small. In that case, the enhancement caused by the bubbles should be close to zero, and the system should be described with $\zeta_I \simeq 0$. In other words, if the negative charges causing ζ_I were in the water, the enhancement of C_{EK} compared to the saturated state would be non-zero, as long as the air–water interface would remain fixed. The dynamic aspect of the EK response would then induce a maximum enhancement with fixed bubbles, and no enhancement obtained with flowing bubbles. This is not the case in this article, where we made the assumption that the negative charges remain in the air, leading to an EK coefficient which is more increased for flowing bubbles than for fixed bubbles.

Let us now compare this work to the other models predicting an enhancement of the EK coefficient. These simulations have allowed to investigate the contribution of the fluid-gas interface when the gas phase is distributed in a single capillary. This is a very different approach from the bundle of capillary tubes model which considers several capillaries occupied by a single phase. By developing such model to the case where each capillary can have a different radius, Jackson (2008, 2010) shows that the excess charge density transported by the flow depends on the capillary size distribution, the wettability and the relative importance of the electrical double layer compared to the capillary radius. In the water-wet case, the EK coefficient is shown to be a decreasing function of the air saturation, because the irreducible water in the smaller capillaries contributes to the electrical conductivity without contributing to the streaming current. In the oil-wet case, when the diffuse layer is not negligible compared to the capillary radius, the electrical conductivity is more impacted by the increasing occupancy of oil than the streaming current. In that case, the EK coefficient can be enhanced up to a factor 2 depending on the capillary size distribution, before decreasing to zero at the irreducible saturation. Under certain conditions, by expressing the EK coefficient as

$$C_{\mathrm{EK}} = \frac{Q_e k}{\sigma_r \eta} \tag{44}$$

where Q_e is the electric charge density and k the rock permeability, and by using the Archie's law $\sigma_r = S_w^n$ to express the rock electrical conductivity, Jackson (2010) obtains an enhancement of the EK coefficient in the water-wet case, but specifies that this approach is consistent only if the saturation exponent is $n = 1$, and that it does not apply to all geologic porous media.

Jougnot *et al.* (2012) also obtain an enhancement of the EK coefficient with a non-monotonous behaviour. Using eq. (44) extended at partial saturation to calculate the EK coefficient, they express the charge density as a flux-averaged quantity, which is defined using the charge density at water saturation, the velocity of the electrolyte and a capillary size distribution. The capillary size distribution is inferred from soil properties using either capillary pressure-saturation relationships or relative permeability functions. Depending on the soil characteristics (porosity, permeability, irreducible saturation), they can obtain a decreasing C_{EK} with decreasing S_w or a non-monotonous trend with an enhancement compared to the saturated state up to a factor 5, consistent with experimental and field measurements. The enhancement of the EK coefficient is there again related to the rock texture.

These works allow to capture petrophysical features which are not possible to study with the present simulations, such as the effect of irreducible saturation and capillary size distribution. They do not consider a non-zero ζ_I potential at the air–water interface.

Another element, which deserves to be studied if the fluid-gas interface contribution is considered as significant, is the behaviour of the interfacial area. In the topology of real porous media, the interconnected pores of the rock networks offer more possibilities to the air phase to spread, merge, and be trapped. It has been reported (Allègre *et al.* 2015) according to both experimental and numerical studies (Culligan *et al.* 2004; Porter *et al.* 2009) that the air–water interfacial area during drainage experiments is a non-monotonous function of S_w. Such behaviour could reinforce the decrease of C_{EK} at low S_w, which is weak in these single capillary model simulations, where the interfacial area increases with decreasing S_w or remains roughly constant.

The pressure gradient does not appear to affect the SP response per se, but high flow velocities generated by high pressure drops are able to release entrapped bubbles, and thus modify the EK coefficient enhancement. The value of pressure drop allowing the release of bubbles is determined by the pore size, bubbles sizes and surface tension between the fluids (see Section 4.3). In a realistic rock and for a given pressure drop, the fraction of pores below a critical radius should be in the trapped bubble configurations, while the fraction of pores above the critical radius should be in the flowing bubble configuration, meaning that the impact of the global flow rate on the SP response may be another element determined by the pore size distribution. This opens a new perspective to explain the

change of magnitude in EK coefficient observed in the experiments of Allègre *et al.* (2010), where the lower the dipole, the stronger the SP response. Considering the analysis of the pressures recorded in these experiments, a change of the interface mobilities going down in the column corresponding to a transition of bubble configuration could yield an increase of the SP response. Future work on experimental measurements of the saturation and bubble state during such experiments is needed to confirm this interpretation.

6 CONCLUSIONS

The simulations of this work show that the electrical charge density associated to the gas-water interfaces is a key element of the EK response. These interfaces yield an increase of the EK coefficient compared to the saturated state. With the assumption that the negative charges causing the ζ_1 potential are in the air, this increase is more important for flowing bubbles than entrapped bubbles.

The EK coefficient enhancement generated by fluid-gas interfaces should improve the performance of the SP-based geophysical techniques in unsaturated conditions. This enhancement should affect the estimate of water flux and unsaturated soil hydraulic parameters inferred from SP measurements, whose magnitude is determined by the electrokinetic coupling (Sailhac *et al.* 2004). Some SP observations related to pumping tests and showing an unexplained enhancement of 25 per cent just above the water table may find an explanation in the enhancement of the EK coefficient in unsaturated conditions, rather than assuming a decaying exponential behaviour as a function of the decreasing water saturation (Malama 2014). The transmissivity and storativity inferred from SP observations may thus be better constrained even for a confined heterogeneous aquifer. When using the SP to deduce the hydrothermal zones on volcanoes, the air–water interface should be taken into account since air convection can also be present if the porous medium is sufficiently permeable (Antoine *et al.* 2009). Finally, these results should be accounted for the monitoring of the water alternate gas injections in reservoirs, where the interfaces between injected water and injected gas could explain the peak of the SP signal associated to the water front (Anuar *et al.* 2014).

ACKNOWLEDGEMENTS

This study benefited from the support of the University of Strasbourg, the CNRS, NEEDS-MIPOR and the Direction Informatique (High Performance Computing Department) of the University of Strasbourg.

REFERENCES

Ahrenholz, B., Tölke, J., Lehmann, P., Peters, A., Kaestner, A., Krafczyk, M. & Durner, W., 2008. Prediction of capillary hysteresis in a porous material using Lattice-Boltzmann methods and comparison to experimental data and a morphological pore network model, *Adv. Water Resour.,* **31**(9), 1151–1173.

Allègre, V., Jouniaux, L., Lehmann, F. & Sailhac, P., 2010. Streaming Potential dependence on water-content in fontainebleau sand, *Geophys. J. Int.,* **182,** 1248–1266.

Allègre, V., Jouniaux, L., Lehmann, F. & Sailhac, P., 2011. Reply to the comment by A. Revil and N. Linde on: 'Streaming potential dependence on water-content in fontainebleau sand', *Geophys. J. Int.,* **186,** 115–117.

Allègre, V., Lehmann, F., Ackerer, P., Jouniaux, L. & Sailhac, P., 2012. A 1-D modelling of streaming potential dependence on water content during drainage experiment in sand, *Geophys. J. Int.,* **189,** 285–295.

Allègre, V., Maineult, A., Lehmann, F., Lopes, F. & Zamora, M., 2014. Self-potential response to drainage-imbibition cycles, *Geophys. J. Int.,* **197,** 1410–1424.

Allègre, V., Jouniaux, L., Lehmann, F., Sailhac, P. & Toussaint, R., 2015. Influence of water pressure dynamics and fluid flow on the streaming-potential response for unsaturated conditions, *Geophys. Prospect.,* **63,** 694–712.

Antoine, R., Baratoux, D., Rabinowicz, M., Fontaine, F., Bachelery, P., Staudacher, T., Saracco, G. & Finizola, A., 2009. Thermal infrared image analysis of a quiescent cone on piton de la fournaise volcano: evidence of convective air flow within an unconsolidated soil, *J. Volcanol. Geotherm. Res.,* **183,** 228–244.

Anuar, S., Jaafar, M., Sulaiman, W. & Ismail, A., 2014. Correlation study between streaming potential signal and waterfront progression during water alternate gas (WAG) injection, *J. Appl. Sci.,* **14,** 1959–1965.

Aursjø, O., Løvoll, G., Knudsen, H.A., Flekkøy, E.G. & Måløy, K.J., 2011. A direct comparison between a slow pore scale drainage experiment and a 2D Lattice Boltzmann simulation, *Transp. Porous Media,* **86**(1), 125–134.

Bao, J. & Schaefer, L., 2013. Lattice Boltzmann equation model for multi-component multi-phase flow with high density ratios, *Appl. Math. Modelling,* **37**(4), 1860–1871.

Brothelande, E. *et al.*, 2014. Fluid circulation pattern inside la soufrière volcano (guadeloupe) inferred from combined electrical resistivity tomography, self-potential, soil temperature and diffuse degassing measurements, *J. Volcanol. Geotherm. Res.,* **288,** 105–122.

Buick, J. & Greated, C., 2000. Gravity in a Lattice Boltzmann model, *Phys. Rev. E,* **61**(5), 5307, doi:10.1103/PhysRevE.61.5307.

Chai, Z. & Shi, B., 2008. A novel Lattice Boltzmann model for the Poisson equation, *Appl. Math. Modelling,* **32,** 2050–2058.

Chidichimo, F., De Biase, M., Rizzo, E., Masi, S. & Straface, S., 2015. Hydrodynamic parameters estimation from self-potential data in a controlled full scale site, *J. Hydrol.,* **522,** 572–581.

Connington, K. & Lee, T., 2012. A review of spurious currents in the Lattice Boltzmann method for multiphase flows, *J. Mech. Sci. Technol.,* **26**(12), 3857–3863.

Creux, P., Lachaise, J., Graciaa, A. & Beattie, J.K., 2007. Specific cation effects at the hydroxide-charged air/water interface, *J. Phys. Chem. C,* **111**(9), 3753–3755.

Culligan, K.A., Wildenschild, D., Christensen, B.S., Gray, W.G., Rivers, M.L. & Tompson, A.F., 2004. Interfacial area measurements for unsaturated flow through a porous medium, *Water Resour. Res.,* **40**(12), doi:10.1029/2004WR003278.

Darnet, M., Marquis, G. & Sailhac, P., 2003. Estimating aquifer hydraulic properties from the inversion of surface streaming potential (SP) anomalies, *Geophys. Res. Lett.,* **30**(13), doi:10.1029/2003GL017631.

Darnet, M., Marquis, G. & Sailhac, P., 2004. Modelling streaming potential (SP) signals induced by water movement in the vadose zone, *J. Hydrol.,* **285,** 114–124.

Darnet, M., Marquis, G. & Sailhac, P., 2006. Hydraulic stimulation of geothermal reservoirs: fluid flow, electric potential and microseismicity relationships, *Geophys. J. Int.,* **166,** 438–444.

Davis, J.A., James, R.O. & Leckie, J., 1978. Surface ionization and complexation at the oxide/water interface, *J. Colloid Interface Sci.,* **63,** 480–499.

Doussan, C., Jouniaux, L. & Thony, J.-L., 2002. Variations of self-potential and unsaturated flow with time in sandy loam and clay loam soils, *J. Hydrol.,* **267,** 173–185.

Fiorentino, E.-A., Toussaint, R. & Jouniaux, L., 2016. Lattice Boltzmann modelling of streaming potentials: variations with salinity in monophasic conditions, *Geophys. J. Int.,* **205**(1), 648–664.

Forté, S. & Bentley, L.R., 2013. Effect of hydrocarbon contamination on streaming potential, *Near Surf. Geophys.,* **11**(1), 75–83.

Giampaolo, V., Rizzo, E., Titov, K., Konosavsky, P., Laletina, D., Maineult, A. & Lapenna, V., 2014. Self-potential monitoring of a crude oil-contaminated site (Trecate, Italy), *Environ. Sci. Pollut. Res.,* **21**(15), 8932–8947.

Gong, S., Cheng, P. & Quan, X., 2010. Lattice Boltzmann simulation of droplet formation in microchannels under an electric field, *Int. J. Heat Mass Transfer,* **53**(25), 5863–5870.

Guichet, X., Jouniaux, L. & Pozzi, J.-P., 2003. Streaming potential of a sand column in partial saturation conditions, *J. geophys. Res.,* **108**(B3), 2141, doi:10.1029/2001JB001517.

Gunstensen, A.K., Rothman, D.H., Zaleski, S. & Zanetti, G., 1991. Lattice Boltzmann model of immiscible fluids, *Phys. Rev. A,* **43**(8), 4320, doi:10.1103/PhysRevA.43.4320.

Hase, H., Hashimoto, T., Sakanaka, S., Kanda, W. & Tanaka, Y., 2005. Hydrothermal system beneath Aso volcano as inferred from self-potential mapping and resistivity structure, *J. Volcanol. Geotherm. Res.,* **143,** 259–277.

Hou, S., Shan, X., Zou, Q., Doolen, G.D. & Soll, W.E., 1997. Evaluation of two Lattice Boltzmann models for multiphase flows, *J. Comput. Phys.,* **138**(2), 695–713.

Huang, H., Thorne Jr, D.T., Schaap, M.G. & Sukop, M.C., 2007. Proposed approximation for contact angles in Shan-and-Chen-type multicomponent multiphase Lattice Boltzmann models, *Phys. Rev. E,* **76**(6), 066701, doi:10.1103/PhysRevE.76.066701.

Ishido, T. & Mizutani, H., 1981. Experimental and theoretical basis of electrokinetic phenomena in rock water systems and its applications to geophysics, *J. geophys. Res.,* **86,** 1763–1775.

Jackson, M.D., 2008. Characterization of multiphase electrokinetic coupling using a bundle of capillary tubes model, *J. geophys. Res.,* **113,** B04201, doi:10.1029/2007JB005490.

Jackson, M.D., 2010. Multiphase electrokinetic coupling: Insights into the impact of fluid and charge distribution at the pore scale from a bundle of capillary tubes model, *J. geophys. Res.,* **115,** B07206, doi:10.1029/2009JB007092.

Jougnot, D., Linde, N., Revil, A. & Doussan, C., 2012. Derivation of soil-specific streaming potential electrical parameters from hydrodynamic characteristics of partially saturated soils, *Vadose Zone J.,* **11**(1), 272–276.

Jougnot, D., Linde, N., Haarder, E.B. & Looms, M.C., 2015. Monitoring of saline tracer movement with vertically distributed self-potential measurements at the HOBE agricultural test site, Voulund, Denmark, *J. Hydrol.,* **521,** 314–327.

Jouniaux, L. & Ishido, T., 2012. Electrokinetics in Earth sciences: a tutorial, *Int. J. Geophysics,* **2012,** doi:10.1155/2012/286107.

Jouniaux, L., Pozzi, J.-P., Berthier, J. & Massé, P., 1999. Detection of fluid flow variations at the Nankai trough by electric and magnetic measurements in boreholes or at the seafloor, *J. geophys. Res.,* **104,** 29 293–29 309.

Kallay, N., Cop, A., Chibowski, E. & Holysz, L., 2003. Reversible charging of the ice−water interface. II. Estimation of equilibrium parameters, *J. Colloid Interface Sci.,* **259,** 89–96.

Kirby, B.J. & Hasselbrink, E.F., 2004. Zeta potential of microfluidic substrates: 1. Theory, experimental techniques, and effects on separations, *Electrophoresis,* **25**(2), 187–202.

Kulessa, B., Hubbard, B. & Brown, G.H., 2003. Cross-coupled flow modeling of coincident streaming and electrochemical potentials and application to subglacial self-potential data, *J. geophys. Res.,* **108**(B8), doi:10.1029/2001JB001167.

Kulessa, B., Murray, T. & Rippin, D., 2006. Active seismoelectric exploration of glaciers, *Geophys. Res. Lett.,* **33,** L07503, doi:10.1029/2006GL025758.

Leroy, P., Jougnot, D., Revil, A., Lassin, A. & Azaroual, M., 2012. A double layer model of the gas bubble/water interface, *J. Colloid Interface Sci.,* **388**(1), 243–256.

Linde, N., Jougnot, D., Revil, A., Matthai, S.K., Renard, D. & Doussan, C., 2007. Streaming current generation in two-phase flow conditions, *Geophys. Res. Lett.,* **34,** LO3306, doi:10.1029/2006GL028878.

Lorne, B., Perrier, F. & Avouac, J.-P., 1999a. Streaming potential measurements. 1. Properties of the electrical double layer from crushed rock samples, *J. geophys. Res.,* **104**(B8), 17 857–17 877.

Lorne, B., Perrier, F. & Avouac, J.-P., 1999b. Streaming potential measurements. 2. Relationship between electrical and hydraulic flow patterns from rocks samples during deformations, *J. geophys. Res.,* **104**(B8), 17 879–17 896.

Maineult, A., Jouniaux, L. & Bernabé, Y., 2006. Influence of the mineralogical composition on the self-potential response to advection of KCl concentration fronts through sand, *Geophys. Res. Lett.,* **33**(24).

Maineult, A., Strobach, E. & Renner, J., 2008. Self-potential signals induced by periodic pumping, *J. geophys. Res.,* **113,** B01203, doi:10.1029/2007JB005193.

Malama, B., 2014. Theory of transient streaming potentials in coupled unconfined aquifer-unsaturated zone flow to a well, *Water Resour. Res.,* **50**(4), 2921–2945.

Martys, N.S. & Chen, H., 1996. Simulation of multicomponent fluids in complex three-dimensional geometries by the Lattice Boltzmann method, *Phys. Rev. E,* **53**(1), 743, doi:10.1103/PhysRevE.53.743.

Mauri, G., Williams-Jones, G. & Saracco, G., 2010. Depth determinations of shallow hydrothermal system by self-potential and multi-scale wavelet tomography, *J. Volcanol. Geotherm. Res.,* **191,** 233–244.

Minsley, B.J., Sogade, J. & Morgan, F.D., 2007. Three-dimensional self-potential inversion for subsurface DNAPL contaminant detection at the Savannah River Site, South Carolina, *Water Resour. Res.,* **43,** doi:10.1029/2005WR003996.

Misztal, M.K., Hernandez-Garcia, A., Matin, R., Sørensen, H.O. & Mathiesen, J., 2015. Detailed analysis of the Lattice Boltzmann method on unstructured grids, *J. Comput. Phys.,* **297,** 316–339.

Naudet, V., Revil, A., Rizzo, E., Bottero, J.-Y. & Bégassat, P., 2004. Groundwater redox conditions and conductivity in a contaminant plume from geoelectrical investigations, *Hydrol. Earth Syst. Sci. Discuss.,* **8**(1), 8–22.

Parmigiani, A., Huber, C., Bachmann, O. & Chopard, B., 2011. Pore-scale mass and reactant transport in multiphase porous media flows, *J. Fluid Mech.,* **686,** 40–76.

Perrier, F. & Morat, P., 2000. Characterization of electrical daily variations induced by capillary flow in the non-saturated zone, *Pure appl. Geophys.,* **157,** 785–810.

Perrier, F., Trique, M., Lorne, B., Avouac, J.-P., Hautot, S. & Tarits, P., 1998. Electric potential variations associated with lake variations, *Geophys. Res. Lett.,* **25,** 1955–1958.

Porter, M.L., Schaap, M.G. & Wildenschild, D., 2009. Lattice-Boltzmann simulations of the capillary pressure–saturation–interfacial area relationship for porous media, *Adv. Water Resour.,* **32**(11), 1632–1640.

Pride, S., 1994. Governing equations for the coupled electromagnetics and acoustics of porous media, *Phys. Rev. B: Condens. Matter Mater. Phys.*, **50,** 15 678–15 695.

Pride, S.R., Flekkøy, E.G. & Aursjø, O., 2008. Seismic stimulation for enhanced oil recovery, *Geophysics,* **73**(5), O23–O35.

Qian, D., McLaughlin, J., Sankaranarayanan, K., Sundaresan, S. & Kontomaris, K., 2006. Simulation of bubble breakup dynamics in homogeneous turbulence, *Chem. Eng. Commun.,* **193**(8), 1038–1063.

Revil, A. & Cerepi, A., 2004. Streaming potentials in two-phase flow conditions, *Geophys. Res. Lett.,* **31**(11), doi:10.1029/2004GL020140.

Revil, A., Linde, N., Cerepi, A., Jougnot, D., Matthäi, S. & Finsterle, S., 2007. Electrokinetic coupling in unsaturated porous media, *J. Colloid Interface Sci.,* **313,** 315–327.

Rizzo, E., Suski, B., Revil, A., Straface, S. & Troisi, S., 2004. Self-potential signals associated with pumping tests experiments, *J. geophys. Res.,* **109**(B10), doi:10.1029/2004JB003049.

Sailhac, P., Darnet, M. & Marquis, G., 2004. Electrical streaming potential measured at the ground surface, *Vadose Zone J.,* **3**(4), 1200–1206.

Saunders, J., Jackson, M. & Pain, C., 2006. A new numerical model of electrokinetic potential response during hydrocarbon recovery, *Geophys. Res. Lett.,* **33**(15), doi:10.1029/2006GL026835.

Shan, X. & Chen, H., 1993. Lattice Boltzmann model for simulating flows with multiple phases and components, *Phys. Rev. E,* **47**(3), 1815, doi:10.1103/PhysRevE.47.1815.

Sherwood, J., 2007. Streaming potential generated by two-phase flow in a capillary, *Phys. Fluids,* **19**(5), 053101, doi:10.1063/1.2717847.

Sherwood, J., Xie, Y., van den Berg, A. & Eijkel, J., 2013. Theoretical aspects of electrical power generation from two-phase flow streaming potentials, *Microfluidics Nanofluidics,* **15**(3), 347–359.

Straface, S. & De Biase, M., 2013. Estimation of longitudinal dispersivity in a porous medium using self-potential signals, *J. Hydrol.,* **505,** 163–171.

Straface, S., Rizzo, E. & Chidichimo, F., 2010. Estimation of hydraulic conductivity and water table map in a large-scale laboratory model by means of the self-potential method, *J. geophys. Res.,* **115**(B6), doi:10.1029/2009JB007053.

Sukop, M.C. & Thorne Jr, D.T., 2006. *Lattice Boltzmann Modeling Lattice Boltzmann Modeling: An Introduction for Geoscientists and Engineers,* Spinger.

Swift, M.R., Osborn, W. & Yeomans, J., 1995. Lattice Boltzmann simulation of nonideal fluids, *Phys. Rev. Lett.,* **75**(5), 830, doi:10.1103/PhysRevLett.75.830.

Swift, M.R., Orlandini, E., Osborn, W. & Yeomans, J., 1996. Lattice Boltzmann simulations of liquid-gas and binary fluid systems, *Phys. Rev. E,* **54**(5), 5041, doi:10.1103/PhysRevE.54.5041.

Takahashi, M., 2005. ζ potential of microbubbles in aqueous solutions: electrical properties of the gas-water interface, *J. Phys. Chem. B,* **109**(46), 21 858–21 864.

Thony, J.-L., Morat, P., Vachaud, G. & Le Mouël, J.-L., 1997. Field characterization of the relationship between electrical potential gradients and soil water flux, *C. R. Acad. Sci., Paris,* **325**(5), 317–321.

Van der Graaf, S., Nisisako, T., Schroen, C., Van Der Sman, R. & Boom, R., 2006. Lattice Boltzmann simulations of droplet formation in a t-shaped microchannel, *Langmuir,* **22**(9), 4144–4152.

Vinogradov, J. & Jackson, M., 2011. Multiphase streaming potential in sandstones saturated with gas/brine and oil/brine during drainage and imbibition, *Geophys. Res. Lett.,* **38,** L01301, doi:10.1029/2010GL045726.

Warden, S., Garambois, S., Jouniaux, L., Brito, D., Sailhac, P. & Bordes, C., 2013. Seismoelectric wave propagation numerical modeling in partially saturated materials, *Geophys. J. Int.,* **194,** 1498–1513.

Watanabe, T. & Katagishi, Y., 2006. Deviation of linear relation between streaming potential and pore fluid pressure difference in granular material at relatively high Reynolds numbers, *Earth, Planets Space,* **58**(8), 1045–1051.

Wolf-Gladrow, D.A., 2005. *Lattice Gas Cellular Automata and Lattice Boltzmann Models - An Introduction,* Springer.

Wurmstich, B. & Morgan, F., 1994. Modeling of streaming potential responses caused by oil well pumping, *Geophysics,* **59,** 46–56.

Xie, Y., Sherwood, J., Shui, L., van den Berg, A. & Eijkel, J., 2010. Massive enhancement of streaming potential power by application of two-phase flow, in *Proceedings Power MEMS,* Leuven, pp. 127–130.

Yang, J. & Boek, E.S., 2013. A comparison study of multi-component Lattice Boltzmann models for flow in porous media applications, *Comput. Math. Appl.,* **65**(6), 882–890.

Yang, C., Dabros, T., Li, D., Czarnecki, J. & Masliyah, J.H., 2001a. Measurement of the zeta potential of gas bubbles in aqueous solutions by microelectrophoresis method, *J. Colloid Interface Sci.,* **243**(1), 128–135.

Yang, Z., Dinh, T.-N., Nourgaliev, R. & Sehgal, B., 2001b. Numerical investigation of bubble growth and detachment by the Lattice-Boltzmann method, *Int. J. Heat Mass Transfer,* **44**(1), 195–206.

Zhang, J. & Kwok, D.Y., 2005. A 2D Lattice Boltzmann study on electrohydrodynamic drop deformation with the leaky dielectric theory, *J. Comput. Phys.,* **206**(1), 150–161.

Zheng, L., Lee, T., Guo, Z. & Rumschitzki, D., 2014. Shrinkage of bubbles and drops in the Lattice Boltzmann equation method for nonideal gases, *Phys. Rev. E,* **89**(3), 033302, doi:10.1103/PhysRevE.89.033302.

Zyserman, F., Jouniaux, L., Warden, S. & Garambois, S., 2015. Borehole seismoelectric logging using a shear-wave source: possible application to CO_2 disposal?, *Int. J. Greenhouse Gas Control,* **33,** 82–102.

APPENDIX

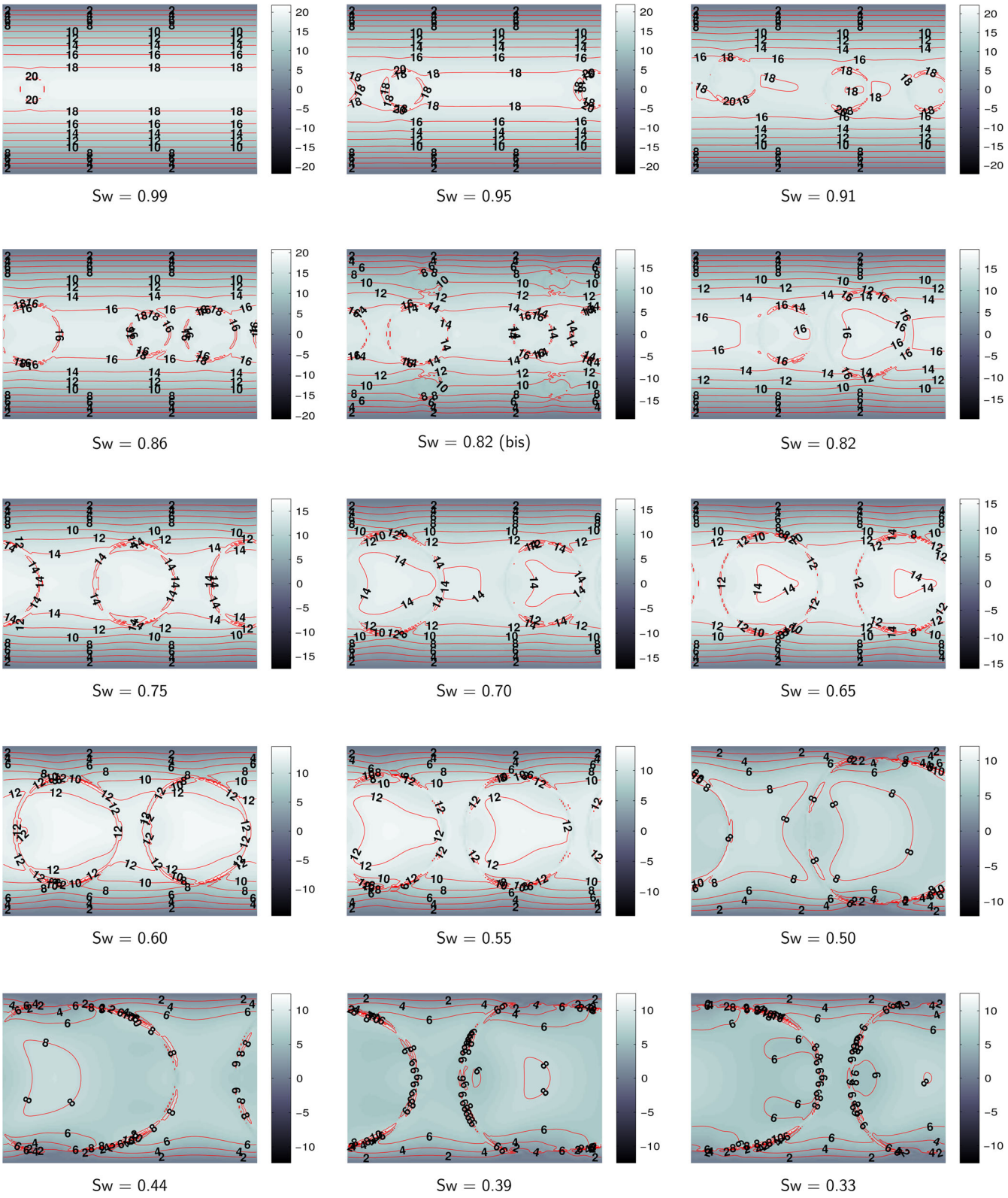

Figure A1. Contour line plots (m s^{-1}) of the velocity fields corresponding to the bubbles shown in Fig. 7.

Table A1. Notation.

Symbol	Description	Unit
	Physical variables	
C_{EK}	Electrokinetic coefficient	V Pa^{-1}
C_i	Local concentration of species i	ions m^{-3}
C_i^{∞}	Concentration of species i in the middle of the channel or out of the sample	ions m^{-3}
χ	Local coordinate measuring the distance to the rock surface	m
d	Debye length	m
δV	Macroscopic potential difference	V
δP	Macroscopic pressure difference	Pa
E	Local electrical field	V m^{-1}
ε_r	Fluid relative permittivity	-
η	Fluid dynamic viscosity	Pa s
k	Rock permeability	m^2
l	Flow characteristic length	m
L	Capillary length	m
μ	Fluid volumetric mass	kg m^{-3}
n	Saturation exponent in Archie's law	-
ν	Fluid kinetic viscosity	m^2 s^{-1}
ψ	Local electrical potential	V
Q_e	Electrical charge density	C m^{-3}
R	Capillary radius	m
Re	Reynold's number	-
S_w	Water saturation	-
σ_r	Rock electrical conductivity	S m^{-1}
σ_f	Fluid electrical conductivity	S m^{-1}
T	Temperature	K
θ	Contact angle	$^{\circ}$
v	Local velocity	m s^{-1}
U	Flow characteristic velocity	m s^{-1}
z_i	Valence of species i	-
ζ_M	Potential of the fluid-rock interface	V
ζ_I	Potential of the fluid-fluid interface	V
	Modelling variables	
c	Lattice velocity	m s^{-1}
dx	Lattice space step	m
dt	Lattice time step	s
D	Artificial diffusion coefficient	m^2 s^{-1}
f_i^{λ}	Local particle distribution function of phase λ in direction i for the velocity calculation	mu lu^{-2} H^{-1}
F_{λ}	Interaction force term exercised on component λ	mu lu^{-1} H^{-1} ts^{-2}
F_{λ}^{ads}	Fluid-solid interaction term in F_{λ}	mu lu^{-1} H^{-1} ts^{-2}
F_{λ}^{coh}	Fluid-fluid interaction term in F_{λ}	mu lu^{-1} H^{-1} ts^{-2}
G^{ads}	Parameter allowing to tune the contact angle	ts^{-1}
G^{coh}	Parameter controlling the magnitude of the surface tension	lu^2 H mu^{-1} ts^{-1}
γ	Surface tension	mu lu H^{-1} ts^{-2}
h_i	Local particle distribution function in direction i for the potential calculation	V
ν^{ad}	Adimensional kinematic viscosity	lu^2 ts^{-1}
P^{ad}	Local adimensional fluid pressure	mu.H^{-1} ts^{-2}
r_B	Bubble radius at equilibrium	lu
ρ	Local total density	mu lu^{-2} H^{-1}
ρ_0	Initial total density	mu lu^{-2} H^{-1}
ρ_{λ}	Local density of component λ	mu lu^{-2} H^{-1}
ρ_e	Local electrical charge density	C m^{-3}
τ_{λ}	Relaxation time of component λ	ts
u_{λ}	Local velocity of component λ	lu ts^{-1}
u_{λ}^{eq}	Local velocity used in the equilibrium distribution	lu ts^{-1}
u'	Local composite velocity of the mixture	lu ts^{-1}
u	Local total velocity	lu ts^{-1}
s_i	Flag variable of the lattice site i	-
w_i	Weights of the equilibrium distribution	-
	Physical constants	
e	Fundamental charge	C
ε_0	Vacuum permittivity	F m^{-1}
k_B	Boltzmann constant	J K^{-1}